Journal of Sedimentary Research

Journal of Sedimentary Research, 2020, v. 90, 1–19
Research Article
DOI: http://dx.doi.org/10.2110/jsr.2020.24

LACUSTRINE CYCLICITY IN THE EARLY EOCENE GREEN RIVER FORMATION, UINTA BASIN, UTAH: EVIDENCE FROM X-RAY FLUORESCENCE CORE SCANNING

ANDREW P. WALTERS,[1] STEPHEN R. MEYERS,[1] ALAN R. CARROLL,[1] TINA R. HILL,[2] AND MICHAEL D. VANDEN BERG[3]
[1]*Department of Geoscience, University of Wisconsin–Madison, 1215 West Dayton Street, Madison, Wisconsin 53706, U.S.A.*
[2]*Bruker Nano, Inc., 5465 East Cheryl Parkway, Madison, Wisconsin 53711, U.S.A.*
[3]*Utah Geological Survey, 1594 W. North Temple, Suite 3110, Salt Lake City, Utah 84114, U.S.A.*

ABSTRACT: **The Green River Formation preserves an extraordinary archive of terrestrial paleoclimate during the early Eocene Climate Optimum (EECO; ∼ 53–50 Ma), expressing multiple scales of sedimentary cyclicity previously interpreted to reflect annual to Milankovitch-scale forcing. Here we utilize X-ray fluorescence (XRF) core scanning and micro X-ray fluorescence (micro-XRF) scanning in combination with radioisotopic age data to evaluate a rock core record of laminated oil shale and carbonate mudstone from Utah's Uinta Basin, with the parallel objectives of elucidating the paleo-environmental significance of the sedimentary rhythms, testing a range of forcing hypotheses, and evaluating potential linkages between high- and low-frequency forcing. This new assessment reveals that the ∼ 100-µm-scale laminae—the most fundamental rhythm of the Green River Formation—are most strongly expressed by variations in abundance of iron and sulfur. We propose that these variations reflect changes in redox state, consistent with annual stratification of the lake. In contrast to previous studies, no support was found for ENSO or sunspot cycles. However, millimeter- to centimeter-scale rhythms—temporally constrained to the decadal to centennial scale—are strongly expressed as alternations in the abundance of silicate- versus carbonate-associated elements (e.g., Al and Si vs. Ca), suggesting changes in precipitation and sediment delivery to the paleo-lake. Variations also occur at the meter scale, defining an approximate 4 m cycle interpreted to reflect precession. We also identify punctuated intervals, associated principally with one phase of the proposed precession cycle, where Si disconnects from the silicate input. We propose an alternative authigenic or biogenic Si source for these intervals, which reflects periods of enhanced productivity. This result reveals how long-term astronomical forcings can influence short-term processes, yielding insight into decadal- to millennial-scale terrestrial climate change in the Eocene greenhouse earth.**

INTRODUCTION

Annual sedimentary laminae, commonly known as varves, are regularly observed in Holocene lake deposits, where their mode of formation can often be directly examined in the context of ongoing sedimentary processes (Glenn and Kelts 1991). Composed of alternating laminae of varying composition and color, varves can be useful in reconstructing detailed lacustrine chronologies. Fine-scale (< 1 mm) laminae are also observed in many ancient lake deposits, but an annual origin is often more difficult to demonstrate conclusively. The early Eocene Green River Formation (Figs. 1, 2) contains some of the best-known pre-Quaternary lacustrine laminites, which typically consist of light-colored carbonate-rich layers that alternate with dark-colored organic-rich layers at the 100–200 micrometer scale (Fig. 3) (Bradley 1929; Washburn et al. 2015).

These Green River Formation laminites (Fig. 3) offer a potentially invaluable archive of the early Eocene greenhouse climate, which reached the peak of Cenozoic warmth at the early Eocene Climatic Optimum (EECO; ∼ 53–50 Ma) (Zachos et al. 2001, 2008; Smith et al. 2008). The oil shale of the Green River Formation has been a subject of keen interest for nearly a century, and has been interpreted to reflect a range of temporal variability spanning annual, subdecadal (2–8 year), quasidecadal (8–18 year), and longer (20–2400 ky) timescales (Sayles 1922; Bradley 1929; Fischer and Roberts 1991; Ripepe et al. 1991; Cole 1998; Machlus et al. 2008; Meyers 2008; Aswasereelert et al. 2013). Based on an assumed annual origin for laminae, these variations have previously been attributed to the El Niño Southern Oscillation (ENSO), sunspot cycles, and Milankovitch-band orbital perturbations (Bradley 1929; Crowley et al. 1986; Ripepe et al. 1991). However, many aspects of these lamina—including whether they are truly annual—remain unknown, largely due to the small spatial scale of the individual laminae. Key questions include laminae composition, lateral continuity, and connections to physical, chemical, and biologic limnologic processes occurring in the paleo-lake.

This study aims to improve this understanding through a sub-millimeter-scale stratigraphic assessment of the elemental and compositional variability of the Green River Formation laminated oil shale and carbonate mudstone facies. Objectives include elucidating the paleo-environmental significance of its sedimentary rhythms, testing the previously hypothesized range of climatic forcing hypotheses, and evaluating potential linkages between short-term (annual to millennial) and long-term (Milankovitch) depositional cyclicity.

Published Online: Month 2020
 1527-1404/20/090-000

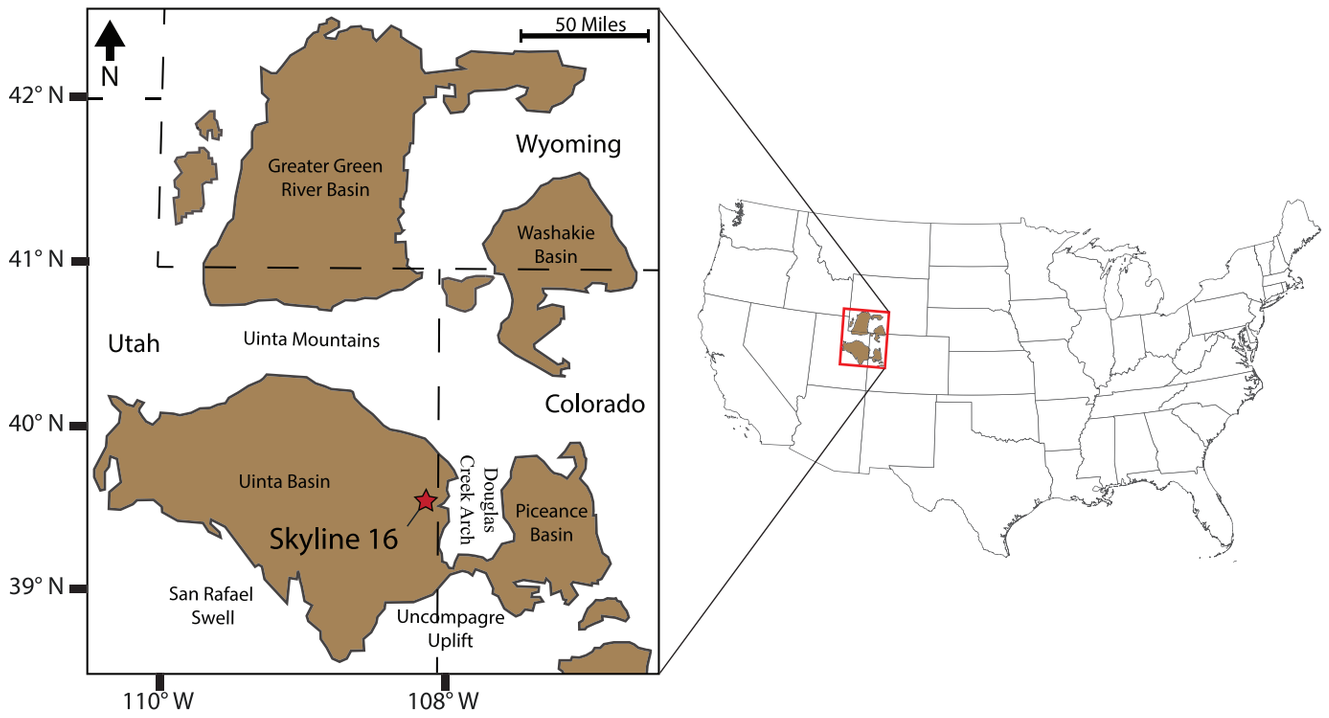

FIG. 1.—Location map of the Green River Formation of Wyoming, Utah, and Colorado. The brown shading represents areas where the Green River Formation is present in outcrop or in the subsurface. The location of the Skyline 16 core is marked by a red star (39° 52′ 14.329″ N, 109° 6′ 44.212″ W). Figure modified from Birgenheier and Vanden Berg (2011).

GEOLOGIC SETTING

The Green River Formation accumulated over approximately 12 million years in the early Eocene (~ 54–43 Ma) in a network of mid-latitude, mid-continental, intermittently saline and alkaline lakes (Sheliga 1980; Remy 1992; Smith et al. 2008). Green River Formation strata were mainly deposited in four depositional basins, the Uinta Basin (northeast Utah), the Greater Green River Basin (southwest Wyoming), the Fossil Basin (southwest Wyoming), and the Piceance Basin (northwest Colorado) (Fig. 1). Structural formation of these basins started in the Late Cretaceous when the Laramide Orogeny began to produce a series of basement-cored anticlinal uplifts in the region east of the Cordilleran fold and thrust belt (Dickinson et al. 1988; Cashion 1995; Rhodes et al. 2002; Smith et al. 2008). Flat slab subduction of the Farallon Plate under the North American Plate is thought to have been the driver of this deformation (Coney and Reynolds 1977; Dickinson and Snyder 1978; Smith et al. 2014). Each Green River Formation depositional basin has a different morphology and depositional character; for example, the Piceance Basin is smaller and deeper than the Uinta Basin, while the Greater Green River Basin is shallower and broader (Rosenberg et al. 2015).

This study focuses on the Uinta Basin, which is confined by the Uinta Mountains in the north, the San Rafael Swell in the southwest, the Uncompahgre Uplift to the southeast, and the Douglas Creek Arch to the east (Fig. 1) (Abbott 1957; Johnson, R.C., 1984; Johnson 1985; Johnson and Brownfield 2015). For periods of the region's history, lake water levels in the Uinta Basin and the adjoining Piceance Basin overtopped the Douglas Creek Arch to form a unified and connected water body termed Lake Uinta (Surdam and Stanley 1980; Smith et al. 2008; Davis et al. 2008; Davis et al. 2009; Tanavssu-Milkeviciene and Sarg 2012; Johnson et al. 2018).

In each Green River Formation depositional basin, a diverse assemblage of lithofacies resulted from highly variable depositional environments (Smith and Carroll 2015). In the Uinta Basin, the Green River Formation has been divided stratigraphically into lower, middle, and upper members (Fig. 2) (Weiss et al. 1990; Witkind 1995; Morgan et al. 2003; Rosenberg et al. 2015). The lower member is composed of the lacustrine carbonate Uteland Butte Member, overlain by the fluviodeltaic tongues of the Wasatch Formation and Colton Formation (also called the Castle Peak Member), and capped by the lacustrine carbonates of the Long Point Bed and Carbonate Marker Unit (Fig. 2) (Abbott 1957; Ryder et al. 1976; Weiss et al. 1990; Morgan et al. 2003; Birgenheier and Vandenberg 2011; Rosenberg et al. 2015; Johnson et al. 2019). The middle and upper members of the Green River Formation are composed of the Douglas Creek Member and the overlying Parachute Creek Member (Fig. 2) (Rosenberg et al. 2015). The Douglas Creek Member is principally fluvial–deltaic with minor intervals of carbonate, while the Parachute Creek Member is predominantly lacustrine carbonate (Birgenheier and Vanden Berg 2011; Rosenberg et al. 2015).

Due to the considerable variation in the organic richness of Parachute Creek Member carbonate mudstone, this unit is subdivided into alternating organic-rich (R) and organic-lean (L) zones (Fig. 2) (Donnell and Blair 1970; Cashion and Donnell 1972; Birgenheier and Vanden Berg 2011). The "Upper R-6" zone, the focus of this study (Fig. 2), was deposited in an expanded, moderately saline lake (Vanden Berg and Birgenheier 2017) under balanced-fill conditions (cf. Carroll and Bohacs 1999), in which input of sediment and water were approximately equivalent to potential basin accommodation (Smith et al. 2008; Birgenheier and Vanden Berg 2011). The overlying "Mahogany zone" (R-7), one of the most organic-rich intervals of the Parachute Creek Member, marks the maximum depth and expansion of the lake and serves as the boundary between the middle and upper Green River Formation members (Johnson 1985; Birgenheier and Vanden Berg 2011; Tanavsuu-Milkeviciene and Sarg 2012; Johnson and Brownfield 2015).

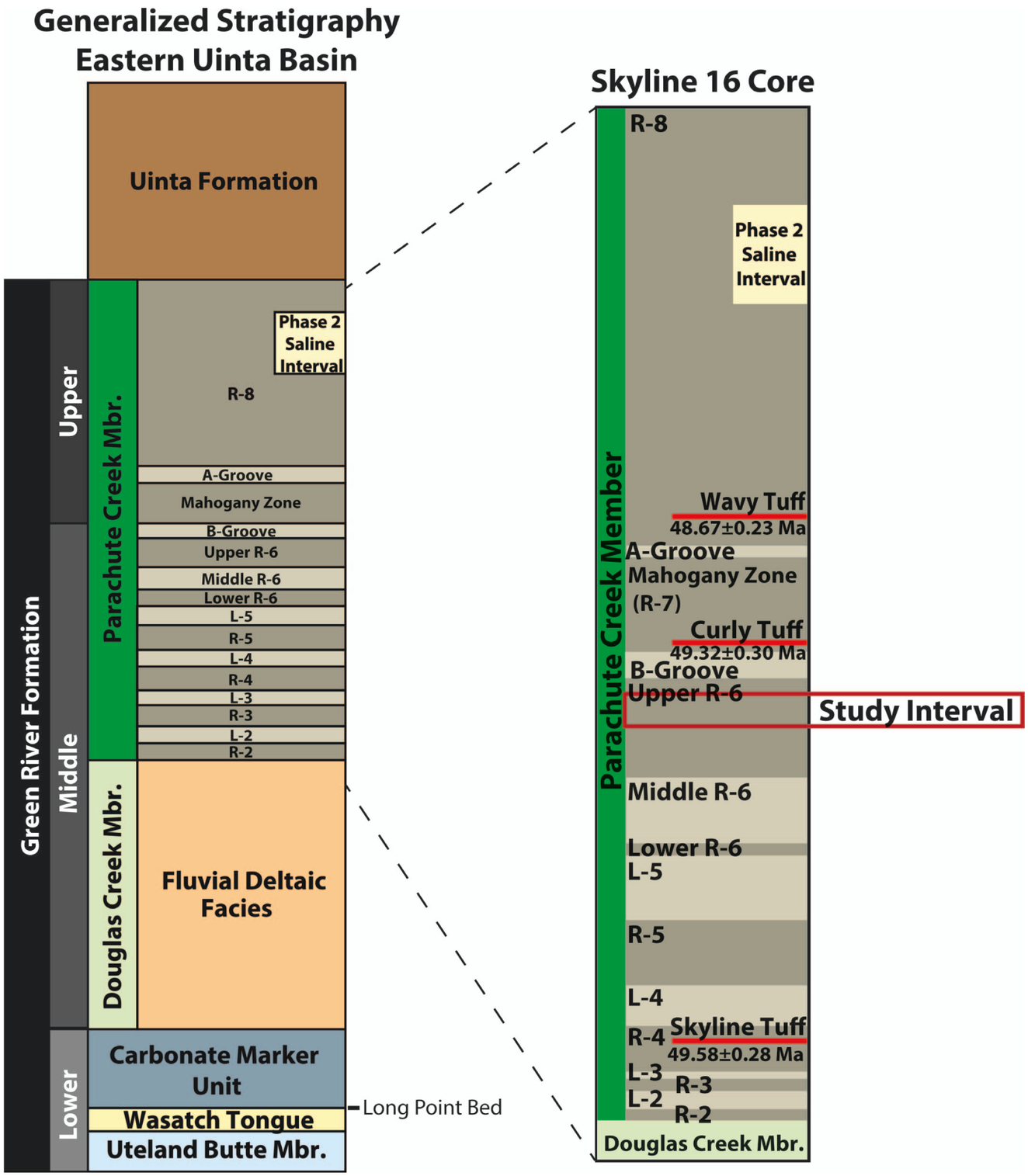

FIG. 2.—The stratigraphy of the Skyline 16 core in the context of the generalized stratigraphy for the Green River Formation in the eastern Uinta Basin. The study interval, marked within a red box, lies in the Upper R-6 zone of the Parachute Creek Member of the Green River Formation at 170.6–179.8 m (560–590 ft) core depth. Modified from Vanden Berg and Birgenheier (2016), Vanden Berg and Birgenheier (2017), Johnson et al. (2018), and Birgenheier et al. (2019).

FIG. 3.—Laminated mudstone in the Upper R-6 zone of the Parachute Creek Member of the Green River Formation captured in the Skyline 16 core. This interval was studied using the 100 micrometer capabilities of the Avaatech XRF core scanner and the 25 micrometer resolution capabilities of the Bruker M4 micro-XRF. Included for comparison are examples of laminites from the Laney Member (Arco Washakie Basin 1 Drill Core: Section 17 T14N R99W) and Wilkins Peak Member (Breathing Gulch Site: 41° 48.50′ N, 109° 17.64′ W) of the The Green River Formation in Greater Green River Basin of Wyoming.

TABLE 1.—Results for ICP elemental calibration of XRF core scanner data at 5 mm resolution.

Proxy	Calibration Equation	R^2 Value	Samples
Al	$y = 0.0002(x) + 0.767$	0.78139	38
Si	$y = 7*10^{-5}(x) + 1.5234$	0.79192	38
K	$y = 2*10^{-5}(x) + 0.2022$	0.94409	38
Ca	$y = 1*10^{-5}(x) + 2.0271$	0.80238	38
Fe	$y = 1*10^{-5}(x) + 0.2643$	0.5616	38
Sr	$y = 0.0061(x) + 150.87$	0.8619	38

TABLE 2.—Results for ICP elemental calibration of XRF core scanner data at 100 micrometer resolution.

Proxy	Calibration Equation	R^2 Value	Samples
Al	$y = 0.001(x) + 1.3373$	0.6882	37
Si	$y = 0.0005(x) + 1.1549$	0.97111	37
K	$y = 0.0001(x) + 0.3464$	0.99302	37
Ca	$y = 6*10^{-05}(x) + 2.5665$	0.99341	37
Fe	$y = 5*10^{-05}(x) + 0.2698$	0.99729	37
Sr	$y = 0.0223(x) + 127.28$	0.95534	37

METHODS

Skyline 16 Core

The Utah Geological Survey and the University of Utah drilled the 10-cm-diameter Skyline 16 core in 2010, sampling ~ 300 m of lacustrine and deltaic facies preserved near the present eastward limit of Uinta Basin lacustrine strata (Figs. 1, 2) (Vanden Berg and Birgenheier 2011; Vanden Berg and Birgenheier 2016). The core extends from the R-8 interval at the top of the Parachute Creek Member, downward to the top of the underlying Douglas Creek Member (Fig. 2). Down-hole well log data, including gamma-ray logs, were also collected from the Skyline 16 borehole. The present study focuses on a 9.2 m section of thinly laminated oil shale and carbonate mudstone facies in the organic-rich Upper R-6 zone in the Parachute Creek Member of the Green River Formation, spanning 170.6–179.8 m core depth (Fig. 2).

XRF Scanning

A third-generation Avaatech X-ray fluorescence (XRF) core scanner at the University of Wisconsin–Madison was used to measure elemental intensities at two down-core resolutions. Core samples were placed slab face up in the scanner, cleaned of debris, leveled, described, and covered in SPEX 3525 Ultralene foil. A continuous down-core measurement path was chosen for each individual core segment to target representative facies and, when possible, avoid any irregularities in the core. A continuous 5-millimeter-resolution (5 mm × 5 mm window size) scan captured millimeter- to meter-scale variations in elemental intensity across the 9.2 m study section of the core. For a 202.6 mm sub-section of this 9.2 m interval (171.47–171.67 m depth; Fig. 4), a second high-resolution scan was completed at a continuous 100 micrometer resolution (0.1 mm × 2 mm window size). This scan aimed to resolve elemental intensity variations at the lamina to near-lamina scale.

To measure a wide range of elements using the XRF core scanner, instrument settings were optimized into two down-core scans per individual core section for both the 5 mm and 100 μm resolution assessments. For 5-mm-resolution evaluations, an acceleration voltage of 10 kV (1200 μA source current, no filter, 20 second measurement time) was used to optimally measure elements in the range of Mg-Fe, while an acceleration voltage of 30 kV (1600 μA source current, thin palladium filter, 20 second measurement time) was used to measure elements Cu–U. For 100-μm-resolution XRF measurements, a 10 kV acceleration voltage (2000 μA source current, no filter, 90 second measurement time) was used to optimally measure Mg-Fe, while a 30 kV acceleration voltage (2000 μA source current, thin palladium filter, 90 second measurement time) was used to evaluate Cu–U. X-ray fluorescence spectra were deconvolved to provide the intensities for various elements using a customized deconvolution model in the WinAxil (v. 4.5.2) X-ray analysis software.

Standard samples were analyzed between each scan run of an individual core section (SARM-4) and before and after the complete analysis of each individual core section (JGb-1, JR-1) to evaluate instrument stability (Supplement 1). For each core section measured, replicate measurements were also taken to quantify instrument variation and evaluate reproducibility for each element (Supplements 2–5). Through examining mean coefficients of variation, standard deviation of the coefficient of variation, and cross plots of elemental intensities for all replicate measurements, we identified sixteen elements (Mg, Al, Si, S, K, Ca, Ti, Mn, Fe, Cu, Zn, Rb, Sr, Zr, Mo, Pb) at the 5 mm resolution and seven elements (Al, Si, S, K, Ca, Fe, Sr) at the 100 μm resolution that displayed superior reproducibility (Supplements 2–5).

Inductively coupled plasma mass spectrometry (ICP-MS) and inductively coupled plasma atomic emission spectroscopy (ICP-AES) analyses were used to provide a means of calibrating Avaatech XRF core scanner elemental intensities to elemental weight percent or parts per million values. For 36 XRF analysis sites, samples were drilled to match the 5 mm down-core resolution using a tungsten carbide cutter affixed to a rotary tool, yielding approximately 1 gram of powder from near the surface of the core. For 5 of the 36 sites, sufficient powder was collected to analyze a duplicate sample using ICP-MS and ICP-AES. At SGS Mineral Services, these samples were prepared using a sodium peroxide fusion technique and measured using ICP-MS and ICP-AES, yielding weight percent or parts per million values for 56 elements. Since weight percent or ppm of S could not be evaluated using these techniques, data for S are presented as elemental intensity. Using these 36 calibration points and 5 duplicate measurements, 5-mm-resolution XRF data were calibrated to measured ICP-MS weight percent or parts per million values using a linear regression calibration (Table 1, Supplement 6). Using the "downscaling approach" of Ma et al. (2014), the 100 μm resolution data were calibrated to weight percent by averaging the 100 μm resolution XRF core scanner results into 5 mm bins that match the location and resolution of the 5 mm ICP calibrated-XRF data. These two measurements were cross-plotted against each other and linearly regressed to produce an ICP-XRF calibration at the 100 μm scale (Ma et al. 2014) (Table 2, Supplement 7).

Micro X-ray fluorescence (micro-XRF) scanning, an elemental-analysis technique that relies on the same principles as XRF core scanning, was also applied to the Skyline 16 core using a Bruker M4 Tornado. This instrument uses polycapillary X-ray focusing optics to create a focal spot of less than 20 μm in diameter, producing a much smaller excitation spot than that of the Avaatech XRF core scanner. The use of high-brilliance focusing X-ray optics, which create a more intense irradiation of the focal spot, produces sufficient fluorescence intensity from sample areas for enhanced trace-element analysis and better resolution of small features.

For this study, a Bruker M4 micro-XRF generated a 25-μm-resolution elemental record for 186.85 mm of the 202.6 mm sub-section of the Skyline 16 study interval (Fig. 5). While the Avaatech XRF core scanner is limited to a resolution of 100 μm, the micro-XRF can measure spot sizes as small as 20 μm, better ensuring that elemental variability at the lamina to sub-lamina scale will be resolved. This instrument measured elemental intensities (in counts) for 20 elements (Na, Mg, Al, Si, S, Cl, K, Ca, Ti, V, Cr, Mn, Fe, Zn, Rb, Sr, Y, Zr, Rh, Ba) under vacuum using two 30 mm^2 detectors and an X-ray source at an acceleration voltage of 50 kV (600 μA source current, 10 ms/pixel, 8 μm step size).

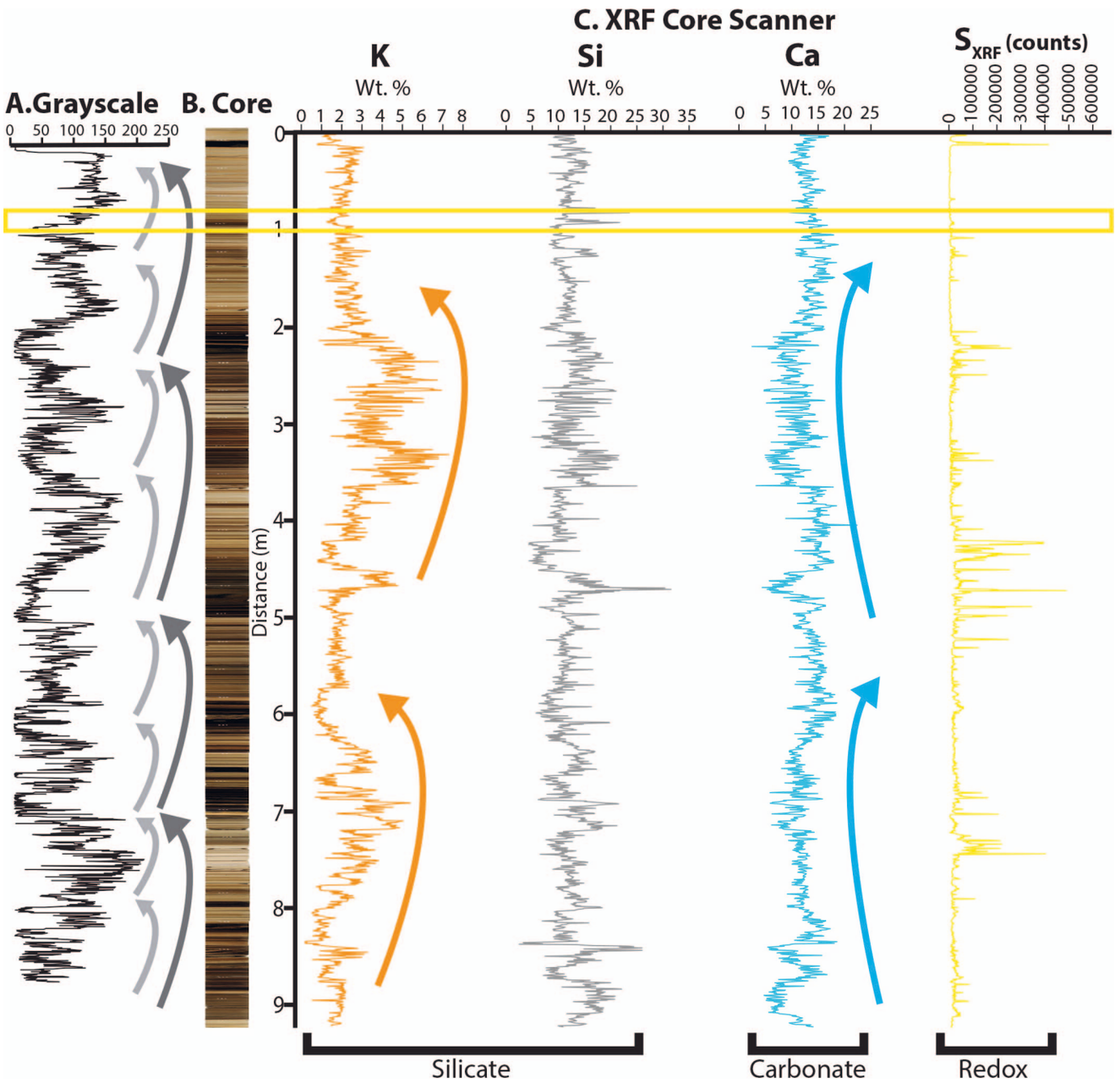

FIG. 4.—5 mm Avaatech XRF core scanner data from the 170.6–179.8 m (560–590 ft) interval of the Skyline 16 core showing **A)** Grayscale values for the study interval, **B)** an image of the core interval, and **C)** selected silicate (K, Si), carbonate (Ca), and redox (S) proxy elements measured using the XRF core scanner. K, Si, and Ca elemental intensities have been converted to wt. % values through calibration with ICP-MS measurements. Arrows represent inferred cyclicity in the 5 mm core record, with the light gray arrows representing the ~ 1 m cycles in grayscale, the dark gray arrows representing the ~ 2 m cycles in grayscale, the orange arrows representing the ~ 4 m cycles in K and blue arrows representing the ~ 5 m cycles in Ca. The 202.6 mm interval studied at higher resolution is outlined in the yellow box.

Grayscale Image Analysis

Grayscale, a type of data which numerically quantifies the light intensity of pixels in an image, was collected for the Skyline 16 core interval. This enabled the comparison of visual lamination, mainly defined by differences in facies brightness, and elemental composition. Intensity values for grayscale measurements range between 0 (Black) and 255 (White). For the 202.6 mm sub-section of the core evaluated with XRF core scanning and micro-XRF, a high-resolution image of the slabbed side of the core was collected using an Epson V500 photo scanner at 3200 dots per inch resolution. Using the National Institute of Health's ImageJ software, grayscale data were collected down the core along the micro-XRF and XRF measurement transects. These transects of grayscale data were then optimally aligned with the high-resolution micro-XRF and XRF data using a sliding correlation algorithm ("slideCor" function in Astrochron; Meyers

TABLE 3.—Correlation results between 100 micrometer XRF core scanner data or 25 micrometer micro-XRF data and grayscale data. Correlations were completed for both the raw data and following removal of pyrite layers in the interval of study.

	MicroXRF (25 µm) Correlation to grayscale	MicroXRF (25 µm) Correlation to grayscale (Pyrite layers removed)	Avaatech (100 µm) Correlation to grayscale	Avaatech (100 µm) Correlation to grayscale (Pyrite layers removed)
Na	0.020	0.020		
Mg	0.496	0.480		
Al	0.014	0.001	–0.210	–0.249
Si	–0.319	–0.33	–0.279	–0.281
S	–0.371	–0.599	–0.557	–0.811
Cl	–0.085	–0.092		
K	0.326	0.314	0.431	0.418
Ca	0.010	0.026	0.120	0.144
Ti	0.066	0.047		
V	0.076	0.068		
Cr	0.055	0.050		
Mn	0.206	0.185		
Fe	0.431	0.605	0.664	0.715
Zn	-0.002	–0.011		
Rb	0.029	0.018		
Sr	0.115	0.106	0.287	0.292
Y	0.014	0.013		
Zr	0.005	0.004		
Rh	–0.047	–0.055		
Ba	–0.265	–0.262		

2014). This correlation was completed with identified pyrite layers both included and excluded (Table 3, Supplement2 8, 9).

Constant-Net-Accumulation-Rate Model

Time-series records were developed from micro-XRF and XRF data using a constant-net-accumulation-rate methodology, which uniformly applies one of three radioisotopically constrained net annual accumulation rates (minimum, nominal, or maximum) across the 202.6 mm study section. This approach makes no assumptions about changes in lamina thickness. Net annual accumulation rates were calibrated using Ar-Ar ages for two volcanic tuff beds that overlie and underlie the study interval. The Skyline Tuff (49.58 ± 0.28 Ma (2σ); Smith and Carroll 2015), located 91 m below the base of the study interval, was sampled directly from the Skyline 16 core and dated by laser fusion of sanidine (Fig. 2). The Wavy Tuff (48.67 ± 0.23 Ma (2σ); Smith et al. 2008; Smith et al. 2010), sampled for Ar-Ar analysis from an outcrop 98 km west of the Skyline 16 core location and dated using incremental heating of biotite, was correlated to 52 m above the top of the study interval (Fig. 2). Using these Ar-Ar ages and their associated 2σ analytical uncertainties, we calculated the minimum, nominal, and maximum net annual accumulation rates for this interval to be 119.8 µm/year, 167.6 µm/year, and 278.4 µm/year, respectively (Table 4). Studies of modern large lakes show that sedimentation rates can vary widely, ranging from 10 to 1000 µm/year (Johnson, T.C., 1984), but our calculated values are well within the range of net annual accumulation rates previously modeled for the Green River Formation based on established Ar-Ar ages (Smith et al. 2003, 2008).

Time-Series Analysis

Using Astrochron (Meyers 2014), a computational package for astrochronologic analysis available for the R statistical computing software (R Core Team 2014), a range of statistical and spectral analysis techniques were applied to the XRF and micro-XRF data. The multi-taper method (MTM), a Fourier technique that uses a specified series of prolate tapers for spectral estimation (Thomson 1982), was used to provide insight into oscillatory variability within a time series record using the "mtm" function in Astrochron (Meyers 2014). To test for a cyclic signal within the noise of the stratigraphic record, the LOWSPEC (locally weighted regression spectral background estimation) technique was applied via the "lowspec" function in Astrochron (Meyers 2012; Meyers 2014). Additionally, evolutive harmonic analysis (EHA), a method which applies MTM to a moving window, was applied using the "eha" function in Astrochron to identify cyclic variability and evaluate potential changes in sedimentation rate (Meyers et al. 2001; Meyers 2014).

RESULTS

Lamina-Scale Results

High-resolution XRF and micro-XRF scanning of the Skyline 16 core permitted analysis of elemental intensities at a previously unattainable resolution for these oil shale and carbonate mudstone facies (Supplement 10). In the 186.5 mm interval of the Skyline 16 core evaluated in high resolution by micro-XRF, several fine-scale elemental trends emerged. Ca, Fe, K, S, and Si all show millimeter-scale variability in elemental composition, while Ca, K, and Si also show distinct centimeter-scale variations in composition (Fig. 5). Millimeter-scale pyrite beds produce the peak elemental intensity values in both Fe and S; however, when looking at other intervals of the micro-XRF record, sub-millimeter-scale variations appear to drive changes in elemental intensity (Fig. 5).

Cross-correlating grayscale with elemental composition, we found that Fe, Mg, and S have the strongest correlation with grayscale in both 25 µm micro-XRF and 100 µm XRF data (Table 3). Higher Fe correlated to lighter color laminae (correlation coefficient = 0.43), while higher S correlated to darker color laminae (correlation coefficient = –0.37). Like Fe, Mg (correlation coefficient = 0.49) was also found to have a strong association with lighter-colored micro-facies, perhaps indicating the presence of Fe- and Mg-rich carbonates in the lighter intervals. Likewise, the association of S with darker-colored intervals appears related to the content of enhanced pyrite and organic matter in these intervals. Other key elements, including Si, Ca, and K, had weaker correlations with grayscale (Table 3). With the removal of pyrite-rich lamina from the record, identified through paired

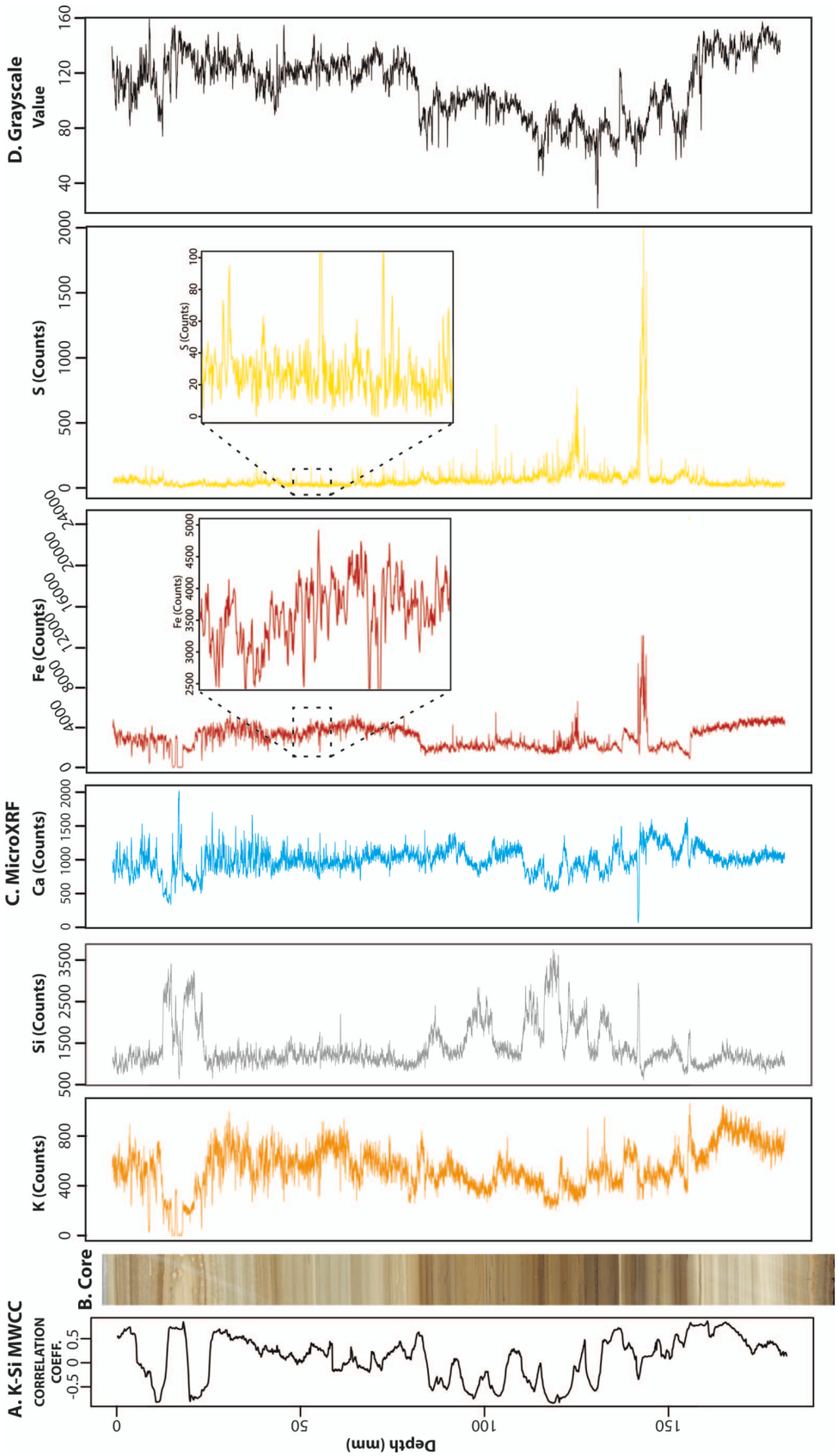

FIG. 5.—Micro-XRF results for the 202.6 mm sub-section of the study interval, showing **A)** the K-Si moving-window cross correlation (window size: 5 mm), **B)** an image of the study section, **C)** the micro-XRF results for K, Si, Ca, Fe, and S, and **D)** grayscale.

TABLE 4.—Criteria for the three testable time series models.

	Minimum Case	Nominal Case	Maximum Case
Constant Net Accumulation Rate Model	119.8 micrometers/yr	167.6 micrometers/yr	278.4 micrometers/yr

high-magnitude peaks in Fe and S elemental intensities, the strength of the correlation of Fe and S to grayscale improved slightly (Table 3). Apart from Mg, the correlation of other elements to grayscale remained comparatively weak (Table 3).

Moving window cross-correlation ("mwCor" function in Astrochron; Meyers 2014) was applied to pairs of micro-XRF records for the entire interval, providing a higher-resolution view of the interrelationship of elements than is possible in a single correlation coefficient (Sageman and Hollander 1999). Use of this technique to compare K and Si, two elements that usually covary, showed punctuated intervals of positive correlation and anti-correlation between the two elements at the millimeter to centimeter scale using a 5 mm moving window (Fig. 5). MTM analysis of this K-Si cross correlation record also identifies millimeter- to centimeter-scale cyclicity, with strong variance present at frequencies between 0 and 0.3 cycles/mm (period: $>$ 3.3 mm/cycle) (Supplement 11). Adjusting the window size of the moving window cross correlation within the range of 3–10 mm consistently shows variance present in the MTM results at millimeter- to centimeter-scale periodicities (Supplement 11).

Following application of minimum (120 μm/year), nominal (168 μm/year), and maximum (278 μm/year) net annual accumulation rates to the micro-XRF record using a "constant net accumulation rate" model (Supplement 12), MTM and LOWSPEC were used to evaluate cyclic variability in these time-series records. Across the range of time models, MTM results for Si show variance that is concentrated above interdecadal ($>$ 15 year) periodicities, with the strongest variance concentrated in the multidecadal (20–100 years), centennial (100–1000 years), and millennial ($>$ 1000 years) bands (Fig. 6). Integrating power across these spectra showed that frequencies between 0 and 0.09 cycles/year (period: $\geq$ 11 years) account for 30–80% of spectral power for the range of temporal models for Si, with much of the power at higher frequencies located in the background (Supplement 13). Taner bandpass filtering of the time-series record was used to visualize this variability and to show the influence of multidecadal- to millennial-scale variability on the Si signal (Fig. 7). Spatially, this variability is expressed as millimeter- to centimeter-scale oscillations in the oil shale.

MTM spectra for S, K, Ca, and Fe time models show comparable results, with variance similarly concentrated in the multidecadal to millennial periodicities (Supplement 14). MTM analyses of Si, S, K, Ca, and Fe time models which were pre-whitened using a LOESS curve display similar interdecadal to millennial variance (Supplement 15), as do LOWSPEC analyses of the Si, S, K, Ca, and Fe time models (Supplement 16). Looking at the higher frequencies, MTM analysis of the range of Si, S, K, Ca, and Fe time models shows low variance within decadal to annual periodicities (approximately 0.1 cycles/year to 1 cycle/year), where ENSO, sunspot, and annual-varve cyclicity are expected to be expressed (Supplement 17). While some frequencies in the quasidecadal to annual range may be statistically significant, none have strong concentrations of spectral power.

Meter-Scale Results

In the 9.2 m core study interval, light- and dark-colored facies alternate at the meter scale (Fig. 4). Grayscale analysis of core images confirms that darker, more organic-rich facies predominate in this interval, with an average grayscale value of 81 on a scale of 0 (Black) to 255 (White). Comparisons of facies color to elemental composition shows an association for several elements; darker-colored facies are generally

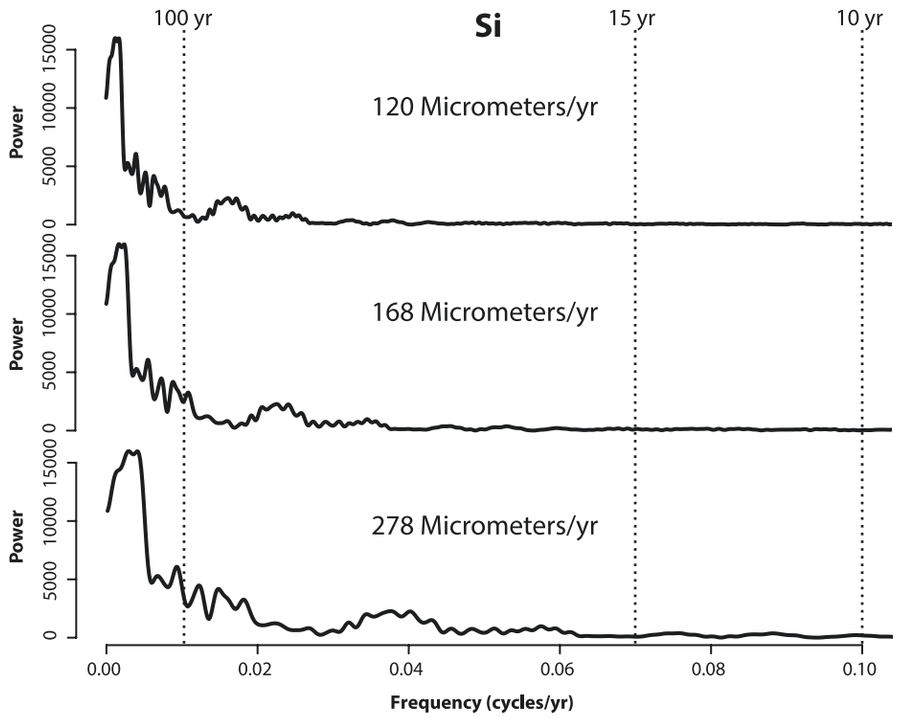

FIG. 6.—MTM results (3-2π DPSS tapers) for Si time models based on application of a constant minimum (120 μm/year), nominal (168 μm/year rate), and maximum (278 μm/year rate) net accumulation rate. Dashed vertical lines highlight approximate 100-year, 15-year, and 10-year periodicities based on the nominal 168 μm/year net accumulation rate.

TABLE 5.—Correlations between elemental intensities in the 5-mm-resolution XRF data.

	Mg	Al	Si	P	S	Cl	K	Ca	Ti	V	Cr	Mn	Fe	Cu	Zn	Br	Rb	Sr	Y	Zr	Mo	Pb	U
Mg	1.00	-0.26	-0.31	-0.21	-0.28	-0.07	0.00	0.17	-0.19	0.11	0.18	0.05	0.02	-0.35	-0.28	-0.02	-0.05	0.15	-0.12	-0.09	-0.33	-0.32	-0.08
Al	-0.26	1.00	0.81	0.08	-0.18	0.02	0.68	-0.84	0.69	0.47	-0.37	0.15	0.46	0.58	0.76	0.03	0.77	-0.76	0.46	0.28	0.21	0.18	-0.10
Si	-0.31	0.81	1.00	0.04	-0.18	0.12	0.48	-0.81	0.60	0.42	-0.38	0.16	0.33	0.43	0.61	0.04	0.64	-0.71	0.35	0.41	0.09	0.13	-0.06
P	-0.21	0.08	0.04	1.00	-0.12	-0.17	0.18	-0.02	0.04	0.04	0.06	-0.08	-0.02	0.11	0.10	-0.09	-0.03	0.24	0.18	0.07	0.09	0.00	0.06
S	-0.28	-0.18	-0.18	-0.12	1.00	-0.28	-0.11	-0.06	-0.06	-0.07	-0.24	0.43	0.10	0.05	-0.03	0.23	-0.09	-0.03	-0.02	0.00	0.14	0.27	0.02
Cl	-0.07	0.02	0.12	-0.17	-0.28	1.00	-0.01	0.04	-0.05	-0.06	0.00	-0.26	-0.17	-0.10	-0.06	0.18	-0.02	-0.01	-0.13	0.01	-0.09	-0.13	-0.02
K	0.00	0.68	0.48	0.18	-0.11	-0.01	1.00	-0.58	0.52	0.26	-0.21	0.11	0.22	0.34	0.51	0.01	0.72	-0.53	0.38	0.13	0.09	-0.08	-0.14
Ca	0.17	-0.84	-0.81	-0.02	-0.06	0.04	-0.58	1.00	-0.70	-0.62	0.44	-0.39	-0.59	-0.63	-0.74	-0.14	-0.76	0.79	-0.49	-0.36	-0.24	-0.30	0.06
Ti	-0.19	0.69	0.60	0.04	-0.06	-0.05	0.52	-0.70	1.00	0.68	-0.28	0.27	0.37	0.61	0.69	0.02	0.77	-0.56	0.54	0.51	0.15	0.19	-0.01
V	0.11	0.47	0.42	0.04	-0.07	-0.06	0.26	-0.62	0.68	1.00	-0.40	0.34	0.52	0.46	0.46	0.09	0.53	-0.40	0.44	0.40	0.09	0.20	0.00
Cr	0.18	-0.37	-0.38	0.06	-0.24	0.00	-0.21	0.44	-0.28	-0.40	1.00	-0.32	-0.24	-0.27	-0.32	-0.16	-0.25	0.37	-0.17	-0.21	-0.11	-0.09	0.02
Mn	0.05	0.15	0.16	-0.08	0.43	-0.26	0.11	-0.39	0.27	0.34	-0.32	1.00	0.31	0.21	0.27	0.10	0.21	-0.32	0.32	0.24	-0.01	0.12	-0.01
Fe	0.02	0.46	0.33	-0.02	0.10	-0.17	0.22	-0.59	0.37	0.52	-0.24	0.31	1.00	0.45	0.41	0.13	0.41	-0.52	0.27	-0.02	0.20	0.41	-0.05
Cu	-0.35	0.58	0.43	0.11	0.05	-0.10	0.34	-0.63	0.61	0.46	-0.27	0.21	0.45	1.00	0.73	-0.01	0.56	-0.46	0.46	0.14	0.53	0.43	0.01
Zn	-0.28	0.76	0.61	0.10	-0.03	-0.06	0.51	-0.74	0.69	0.46	-0.32	0.27	0.41	0.73	1.00	0.01	0.68	-0.59	0.50	0.30	0.30	0.27	-0.05
Br	-0.02	0.03	0.04	-0.09	0.23	0.18	0.01	-0.14	0.02	0.09	-0.16	0.10	0.13	-0.01	0.01	1.00	-0.01	-0.08	-0.01	0.06	0.02	0.25	0.03
Rb	-0.05	0.77	0.64	-0.03	-0.09	-0.02	0.72	-0.76	0.77	0.53	-0.25	0.21	0.41	0.56	0.68	-0.01	1.00	-0.66	0.52	0.40	0.14	0.10	-0.12
Sr	0.15	-0.76	-0.71	0.24	-0.03	-0.01	-0.53	0.79	-0.56	-0.40	0.37	-0.32	-0.52	-0.46	-0.59	-0.08	-0.66	1.00	-0.36	-0.13	-0.11	-0.20	0.13
Y	-0.12	0.46	0.35	0.18	-0.02	-0.13	0.38	-0.49	0.54	0.44	-0.17	0.32	0.27	0.46	0.50	-0.01	0.52	-0.36	1.00	0.41	0.18	0.17	0.04
Zr	-0.09	0.28	0.41	0.07	0.00	0.01	0.13	-0.36	0.51	0.40	-0.21	0.24	-0.02	0.14	0.30	0.06	0.40	-0.13	0.41	1.00	-0.07	0.06	0.03
Mo	-0.33	0.21	0.09	0.09	0.14	-0.09	0.09	-0.24	0.15	0.09	-0.11	-0.01	0.20	0.53	0.30	0.02	0.14	-0.11	0.18	-0.07	1.00	0.48	0.05
Pb	-0.32	0.18	0.13	0.00	0.27	-0.13	-0.08	-0.30	0.19	0.20	-0.09	0.12	0.41	0.43	0.27	0.25	0.10	-0.20	0.17	0.06	0.48	1.00	0.12
U	-0.08	-0.10	-0.06	0.06	0.02	-0.02	-0.14	0.06	-0.01	0.00	0.02	-0.01	-0.05	0.01	-0.05	0.03	-0.12	0.13	0.04	0.03	0.05	0.12	1.00

accompanied by higher K, S, and Si composition, while lighter-colored intervals are typically associated with higher Ca composition (Fig. 4). The association of higher K and Si content with darker-colored facies is consistent with the findings of Robb and Smith (1974), who identified a direct relationship between organic volume and silicate-mineral content in Green River Formation oil shales in Colorado.

In this study interval, composed principally of the oil shale and carbonate mudstone facies, Si and Ca are the two most abundant elemental components. Given that the mineralogy of these facies in the Green River Formation most commonly contains calcite, dolomite, quartz, alkali feldspar, plagioclase, and illite and other clay minerals, we expect Ca composition to generally reflect carbonate mineral content and K and Si to principally reflect silicate-mineral content (Bradley and Eugster 1969; Hosterman and Dyni 1972; Picard and High 1972; Robb and Smith 1974; Dyni 1976). Looking at the interrelationship of different elements in the 5 mm resolution XRF data, we find that Si positively correlates with K (0.484), while Ca negatively correlates with both Si (–0.814) and K (–0.578) (Table 5). This anti-phased relationship reflects meter-scale cyclicity between darker, more silicate-rich and lighter, more carbonate-rich facies (Fig. 4). Washburn et al. (2015) also identified this anti-phased relationship between carbonate and silicate plus organic matter in their Transmission Fourier transform infrared spectroscopy assessment of oil shale samples from the Parachute Creek Member in the Piceance Basin.

In the 5 mm XRF data, K and Ca demonstrate the most coherent multi-meter scale cyclicity. For these two elements, an approximate 4–5 m cycle is visually apparent in the XRF record (Fig. 4). MTM and LOWSPEC analysis of the K record confirms this visually inferred cyclicity, identifying an $\sim$ 4.4 m cycle (frequency: 0.229 cycle/m) and 2 m cycle (frequency: 0.480 cycle/m) (Fig. 8, Supplement 18), while EHA analysis for K shows strong concentrations of power and amplitude at these periodicities across the study interval (Fig. 9). For Ca, MTM, and LOWSPEC analysis identified an $\sim$ 5.1 m (frequency: 0.196 cycle/m) and an $\sim$ 2.13 m (frequency: 0.469 cycle/m) cycle (Fig. 8, Supplement 18). EHA analysis of Ca shows strong concentrations of power and amplitude in this range, with the strongest and most consistent signal in the uppermost 5 meters of the study section (Fig. 9).

While Si generally mirrors K, overall Si shows more dynamic swings in elemental composition and more apparent influence of higher-frequency cycles. MTM and LOWSPEC analysis indicates the presence of an $\sim$ 7 m (frequency: 0.142 cycle/m) cycle and a range of sub-1 m (frequency: $>$ 1 cycle/m) cycles (Fig. 8, Supplement 18). This 7 m cycle in Si is anti-phased with the 5.1 m cycle identified in the Ca record (Fig. 4), a result which is consistent with the negative Pearson correlation coefficient calculated for Si and Ca (Table 5). EHA analysis of this Si record shows strong power and amplitude at the frequencies associated with those periods for much of the study section (Fig. 9).

MTM and LOWSPEC analyses of S indicates the presence of a 1 m (frequency: 1.02 cycle/m) cycle (Fig. 8, Supplement 18). Maxima of this oscillation appear to correspond to periods of high silicate input and darker color (Fig. 4). Based on XRF results, S is associated with both organic material and in iron sulfides. EHA analysis for S showed inconsistent concentrations of power and amplitude at the frequencies associated with these cycles, with the strongest signals shown in intervals of the study section showing the highest S intensity (Fig. 9).

MTM analyses of Si, S, K, and Ca records which were pre-whitened using a LOESS curve display similar results to the untreated data (Supplement 19). EHA plots of gamma-ray-log data (Supplement 20) indicate the presence of peaks in power and amplitude at frequencies similar to those cycles identified in the XRF data through the entire Upper R-6 interval of the Parachute Creek Member in the Skyline 16 core. MTM

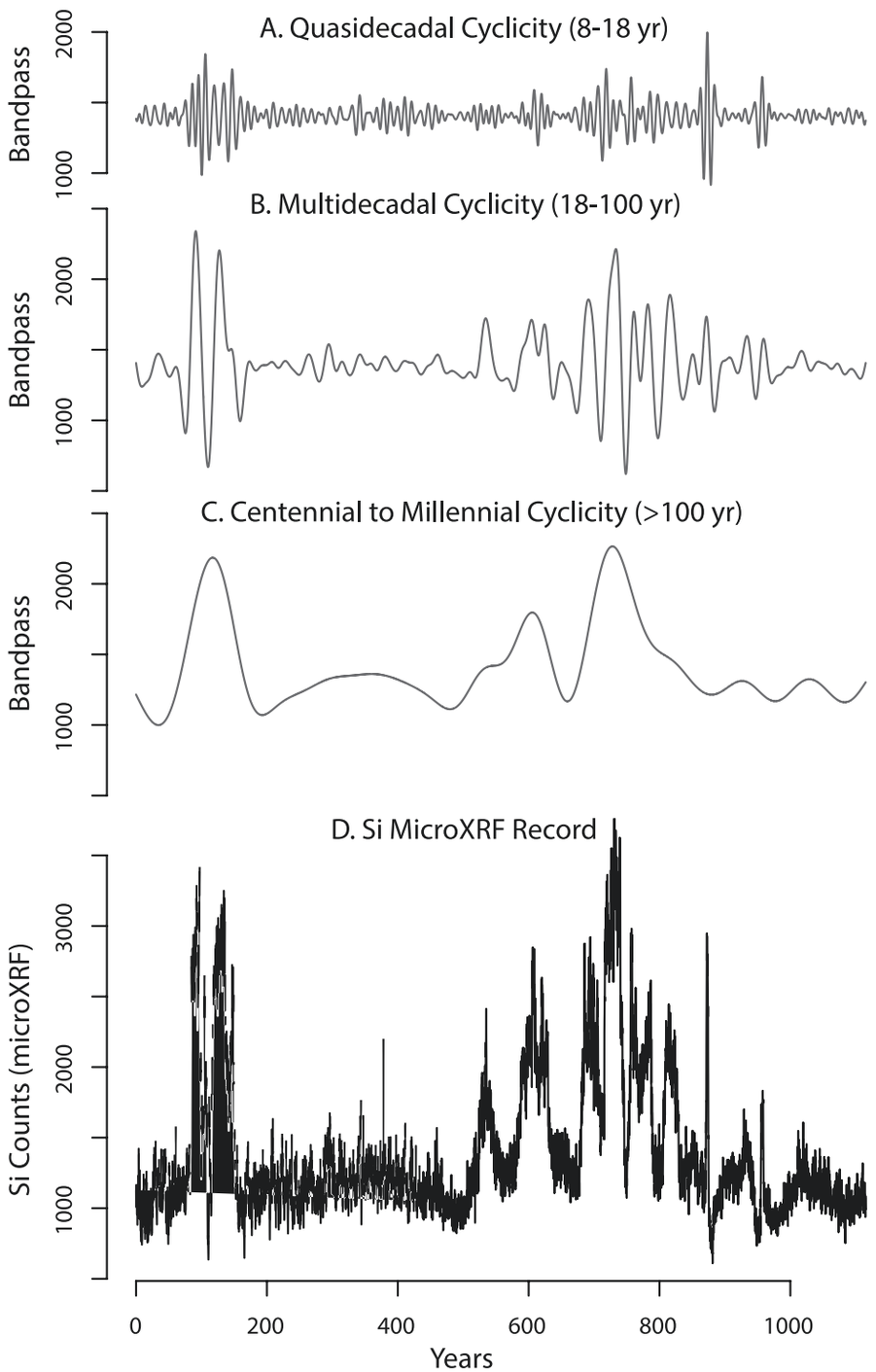

FIG. 7.—Taner bandpass filter of the Si record of the constant sedimentation rate model using the nominal case (167.6 μm/year) net accumulation rate for time scale construction, showing **A)** quasidecadal variability (8–18 years), **B)** multi-decadal variability (18–100 years), **C)** centennial-to millennial-scale variability (> 100 years), and **D)** micro-XRF results for Si for comparison.

and LOWSPEC analysis identified spectral peaks at periods of 15.5 m (frequency: 0.064 cycle/m), and 3.87 m (frequency: 0.258 cycle/m) in the gamma-ray-log data. The shorter of these two cycles is consistent with the 4 m to 5 m cycle identified in the XRF data for Ca and K.

Moving-window cross-correlation of pairs of elemental records was used to identify intervals of positive correlation and anti-correlation ("mwCor" function; Meyers 2014). While the moving-window cross-correlation results for most pairs of elements were consistent with their overall correlation coefficient, Si and K showed punctuated intervals of anti-correlation in the moving-window cross correlation despite an overall positive Pearson correlation coefficient (0.48) (Fig. 10, Table 5). These zones of Si and K anti-correlation include the section of core studied at high resolution using micro-XRF and XRF, where we observed this anti-correlation at the millimeter and centimeter scale (Fig. 5, Supplement 21), but also encompass other parts of the core (Fig. 10). Comparing the moving-window cross-correlation coefficient to the XRF record for K, we observe that anti-correlation events are largely associated with the low-weight-percent phase of the ~ 4 m oscillation in K (Fig. 10). MTM

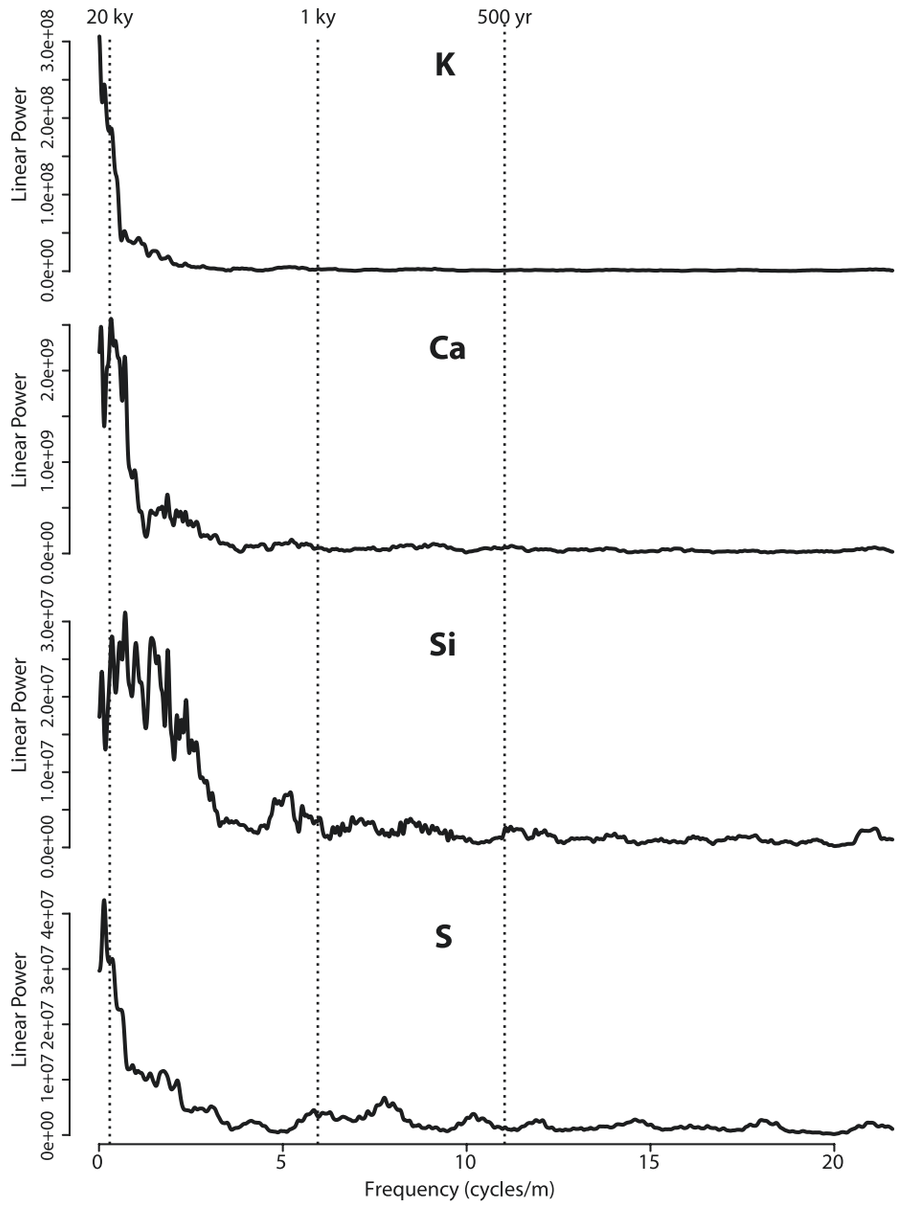

FIG. 8.—MTM power-spectra results (3-2π DPSS tapers) from 5 mm XRF core scanner data for K, Ca, Si, and S. Dashed vertical lines represent approximate 20-ky, 1-ky, and 500-year periodicities based on a 168 μm/year net accumulation rate.

analysis of these K-Si moving-window cross-correlation results calculated using a range of window sizes (50 mm to 0.5 m) supports this observation, identifying an ~ 4.8 m cyclicity and strong variance concentrated at low frequencies (Supplement 21).

DISCUSSION

Spectral analysis of XRF and micro-XRF data reveals multiple scales of cyclicity expressed in various proxy elements, suggesting that different earth system processes are exerting a control on cyclicity at disparate time scales (Fig. 11). Meter-scale cycles are interpreted to reflect the impact of precession-scale change on the flux of allogenic (siliciclastic) vs. autogenic (carbonate) sediment. Centimeter- to millimeter-scale cycles are inferred to be related to decoupling of biogenic silica from the silicate flux and appear to be related to the phase of precession. Sub-millimeter laminae are interpreted to mainly record seasonal change in redox state.

Precessional to Sub-Precessional Modulation of Carbonate vs. Siliciclastic Sedimentation

In the XRF data, we observed oscillations in elemental composition at the multi-meter scale for K, Ca, Si, and S (Figs. 4, 8), which we infer to be related to alternations in carbonate versus silicate fluxes into early Eocene Lake Uinta. Of the cycles identified through spectral analysis, a 4–5 m cycle in both K and Ca is particularly well defined (Figs. 4, 8). Radioisotopically constrained estimates of net annual accumulation rates place the nominal net annual accumulation rate at 168 μm/year, suggesting that each of these ~ 4 m cycles represent approximately 23,000 years. Based on lamina counting (Bradley 1929) and on analysis of well-log and Fischer-assay data (Cole 1998; Machlus et al. 2008; Meyers 2008; Machlus et al. 2015), Green River Formation cycles in the Parachute Creek Member of Colorado and Wilkins Peak Member of Wyoming on the order of 3–5 m have been linked to 21–23 ky precessional periods. In the Upper

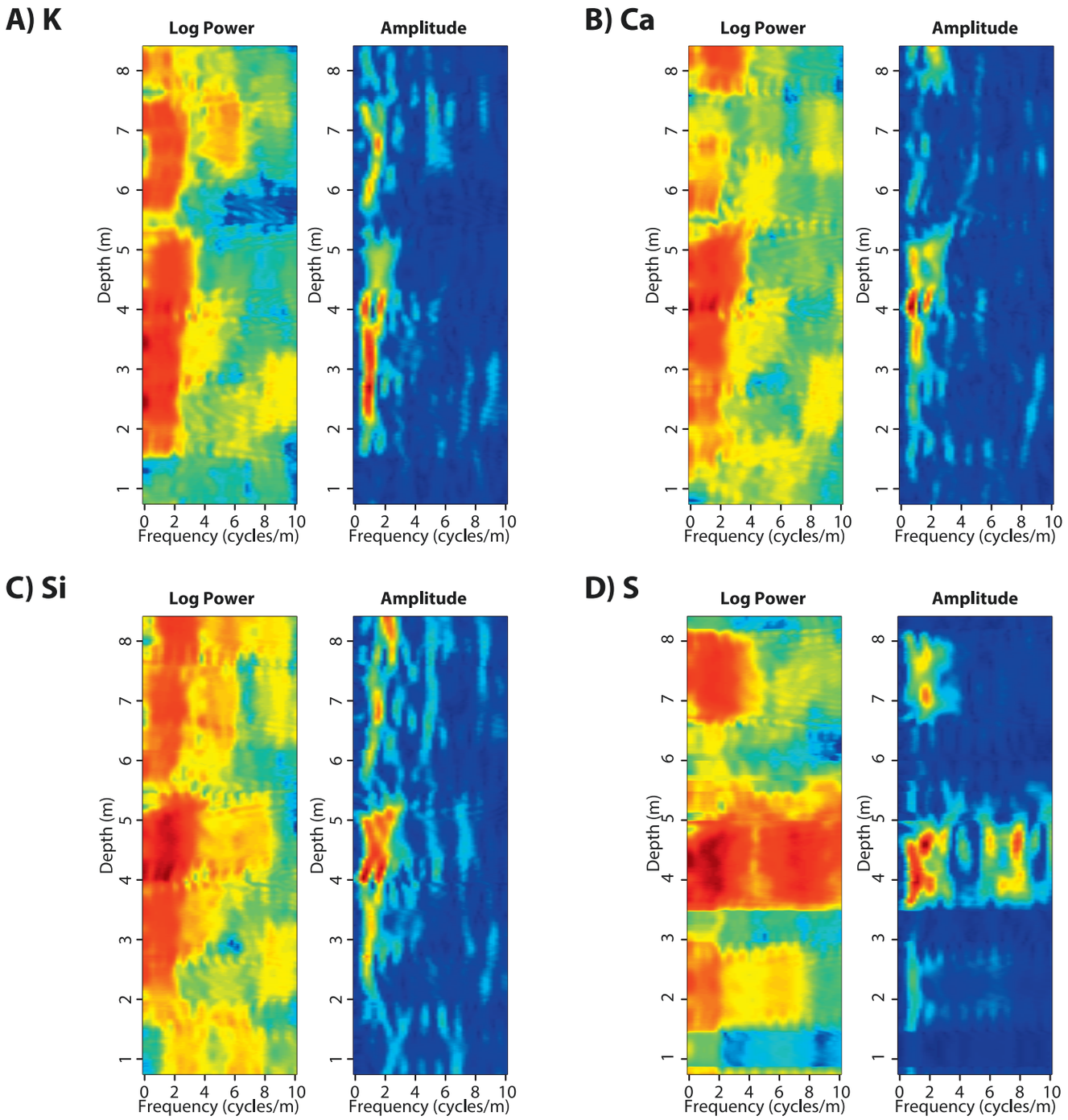

FIG. 9.—EHA plots (3-2π DPSS tapers; window size: 1.5 m) showing log power and amplitude for the 5 mm resolution XRF core scanner record of **A)** K, **B)** Ca, **C)** Si, and **D)** S.

R-6 interval of the Parachute Creek Member studied here, we propose that precession paced a two-component, anti-phased oscillation between autogenic (carbonate dominated) and allogenic (silicate dominated) facies, as reflected in the relative abundances of K and Ca. These facies alternations could result from the influence of precession on the hydrologic system and on productivity, which governed precipitation, sediment, and biological-matter input into the paleo-lake.

Given a nominal 168 μm/year net accumulation rate, the 1 m cyclicity observed in S and the 2 m cyclicity observed in K and Ca may represent sub-precessional cyclicity on the order of 6 ky and 12 ky, respectively. The scale of S cyclicity appears to correspond to the ∼ 1 m and ∼ 2 m scale dark to light color alternations visible in this core section, most easily observed in the grayscale data (Fig. 4). Sub-precessional depositional cycles have previously been noted in the Wilkins Peak Member of the

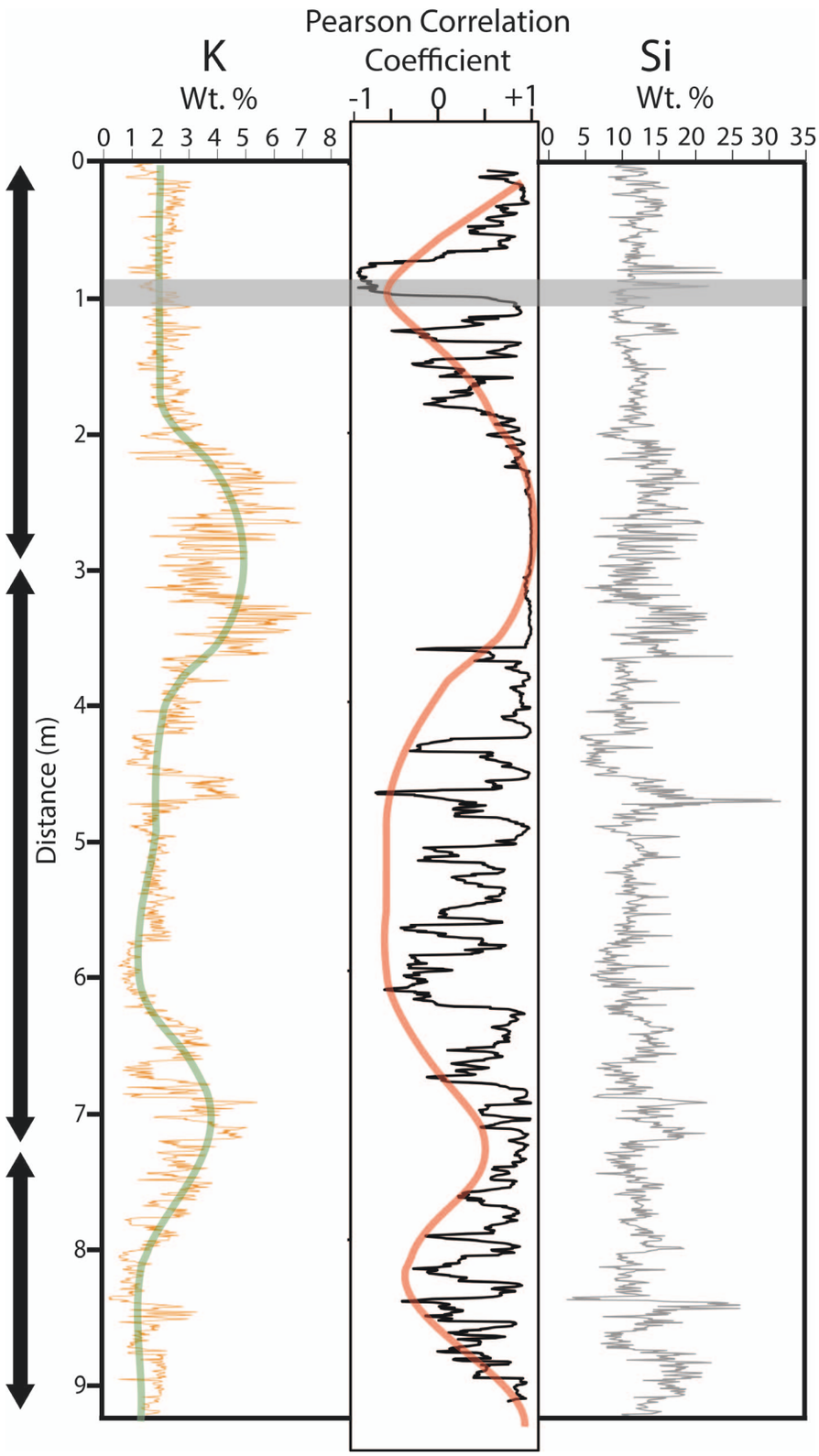

FIG. 10.—Moving-window cross correlation (window size: 0.1 m) of 5 mm resolution XRF core scanner data for K and Si showing the proposed precession beat in K (green line) and the approximate cycle of Si anti-correlation events from the silicate signal (red line). The gray shaded box highlights the interval selected for higher-resolution XRF and micro-XRF analysis.

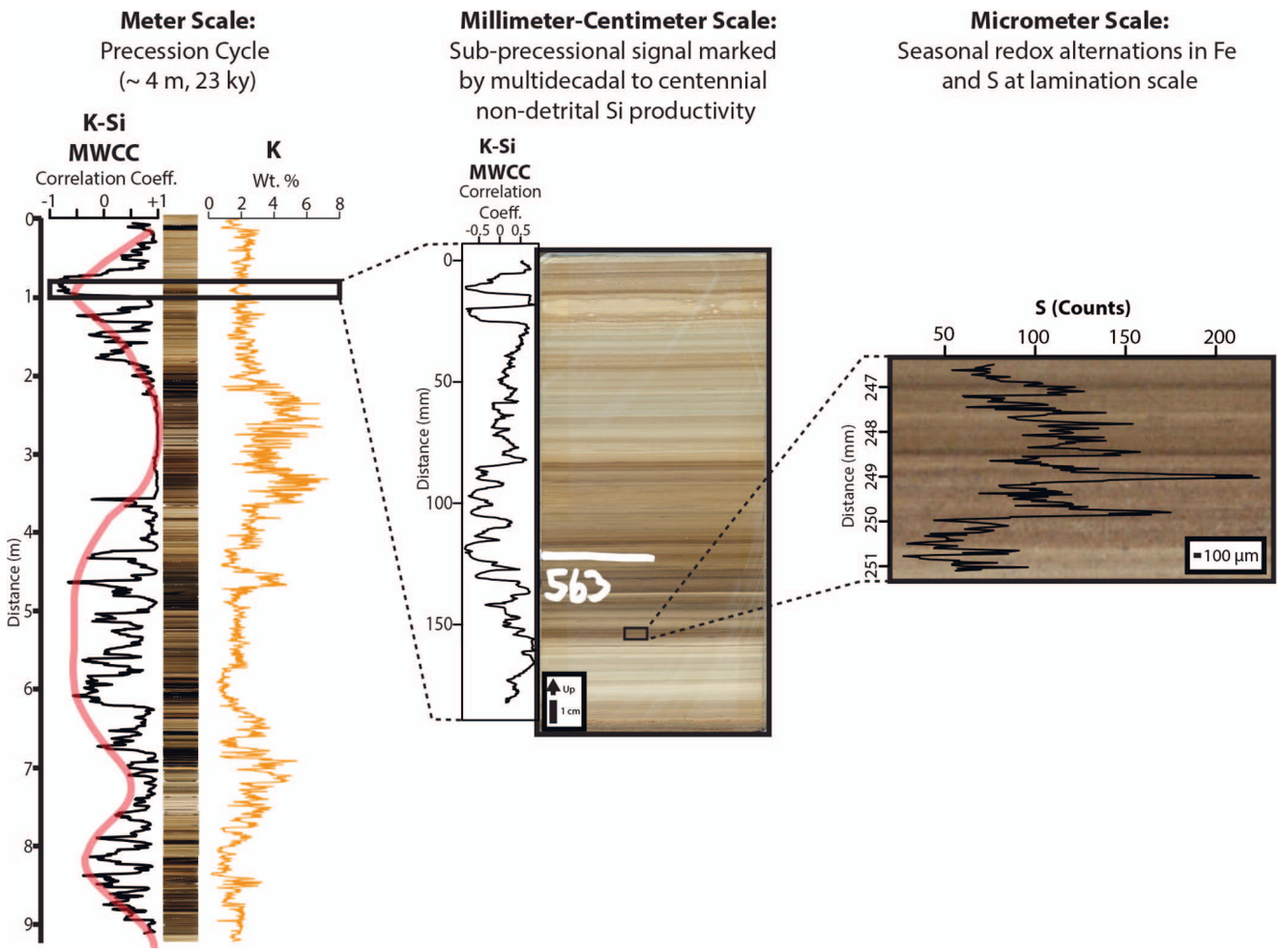

FIG. 11.—Synthesis of cyclicity from the meter scale to the micrometer scale in the Upper R-6 study interval of the Parachute Creek Member, Green River Formation in the Skyline 16 core.

Green River Formation in Wyoming (Pietras et al. 2003; Machlus et al. 2008), but the mechanism for their formation remains unclear. Pietras et al. (2003) suggested that this sub-Milankovitch cyclicity may be related to either depositional system auto-cyclicity connected to regional tectonic and geomorphic controls on drainage network stability or nonlinear climate responses to astronomical forcing. Machlus et al. (2008) declined to attribute the identified sub-Milankovitch cyclicity to a particular source, citing ambiguities in their temporal model which do not permit precise characterization of these cycles.

In the case of S, commonly interpreted to be a redox-sensitive element (e.g., Sageman and Lyons 2003; Sluijs et al. 2008), this sub-precessional cyclicity likely reflects changes in lake-bottom oxygenation. The enrichment of organic matter and pyrite in the S rich intervals of the core likewise suggests lake-bottom anoxia and reducing conditions, which enhanced organic-matter preservation and allowed the formation of pyrite. Additionally, the observation that these S-rich intervals are often coincident with intervals of enhanced Si and K input suggests a silicate–redox connection in the paleo-lake (Fig. 4). Explanations for this association include an increase in nutrient flux from rivers during times of increased silicate input, a reduction in the production of carbonates leading to diminished organic-matter dilution, or an enhancement of organic-matter preservation as the result of ectogenic meromixis, in which the addition of freshwater to the surface waters of the lake acts to strengthen stratification (e.g., Horsfield et al. 1994).

Multi-Decadal to Millennial Decoupling of Siliciclastic vs. Biogenic Silica Input

While XRF data showed that Si and K typically co-vary with changing silicate mineral content (Table 5), application of a moving-window cross correlation (window size: 0.1 m) to these two elements identified intervals of clear centimeter-scale anti-correlation in the 9.2 m study section (Fig. 10). These intervals of anti-correlation are clustered principally in the low K phase of the 4 m oscillation observed in K (Fig. 10). Based on micro-XRF results of this study, this decoupling of Si from other elements associated with siliciclastic influx occurs all the way down to the millimeter to centimeter scale, which temporally equates to multidecadal to millennial cyclicity based on our time-series models (Figs. 6, 7).

This decoupling may reflect input from one of several Si sources. One source of this additional Si could be ash or volcaniclastic material, but this is unlikely given that the Upper R-6 zone in the Skyline 16 core is sparsely populated with tephra (Vanden Berg and Birgenheier 2016). Additionally, detailed examination of the study interval and comparison with XRF spectra for individual measurements across these decoupling events suggest that they generally are not related to tuffs or reworked volcanic detritus.

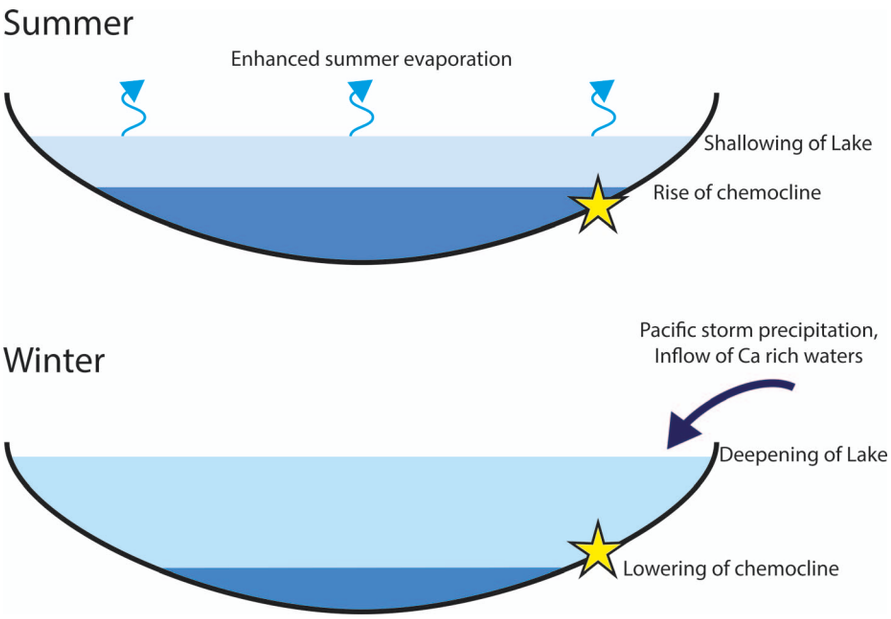

FIG. 12.—Depositional model for the formation of laminae based on results from the Upper R-6 study interval. The location of the Skyline 16 core is marked by a yellow star.

Biological productivity is a second potential source of non-detrital Si in lake systems. In the fossil record of the Green River Formation, however, there is a dearth of preserved siliceous remains. Diatoms, the most common siliceous lacustrine organisms in many modern and ancient lakes, have not yet been identified in the Green River Formation, and previous studies suggest that these organisms may not have proliferated in lakes in western North America until later in the Eocene (Lohman and Andrews 1968; Krebs 1994; Bradbury and Krebs 1995; Mustoe 2005; Wolfe et al. 2006). A biological source of non-detrital Si cannot be definitively ruled out, however. Laboratory experiments and studies of Pleistocene and Holocene saline lakes show that diatom preservation may be reduced in alkaline, saline lake waters (Barker et al. 1994; Ryves et al. 2006; Flower and Ryves 2009; Riemer et al. 2009; North et al. 2018). It is therefore possible that the non-detrital silica we observe could represent the recrystallization of silica from dissolved diatoms.

An authigenic source of Si, however, may also account for non-detrital Si. While silica is more soluble at high pH (Knauss and Wolery 1988; Dove and Rimstidt 1994; Crundwell 2014), a lower-pH environment may allow dissolved silica to recrystallize. In Lake Uinta, pore space near the sediment–water interface could be more restricted, permitting less alkaline conditions than the main body of the lake. Organic-matter decomposition could provide a mechanism for lowering the pH in the pore space of the sediment, thus providing more favorable conditions for the precipitation of authigenic silica. If organic-matter decomposition is driving the changes in pore-water chemistry that periodically enhance authigenic Si deposition, we infer that this signal principally reflects productivity levels in the lake.

The close association of millimeter- to centimeter-scale Si decoupling events with the silicate-poor, carbonate-rich phase of the $\sim$ 4 m proposed precession cycle (Fig. 10) suggests that precessional forcing influenced the timing and expression of these shorter-term cycles. Stimulation of short-lived episodes of enhanced productivity in Lake Uinta through precessional forcing is one mechanism that could generate the authigenic or biogenic silica that appears to drive these decoupling events.

Annual Redox Fluctuation

Spectral analysis of time models for Ca, K, and Si show high concentrations of power at frequencies of less than 0.07 cycle/year (Period: $\geq$ 14 years) (Figs. 6, 7), suggesting that carbonate and silicate deposition evolved with a multidecadal- to precessional-scale cyclicity (Figs. 6–8). In contrast, low concentrations of spectral power are observed at frequencies greater than 0.07 cycles/year (periods: $\leq$ 14 years) (Fig. 6). Therefore, our results in the Upper R-6 zone of the Parachute Creek Member do not support previous studies that interpreted a strong ENSO and sunspot forcing of Green River Formation laminites.

Additionally, despite the apparent lamina-scale variations in Fe and S intensity, no strong concentration of variance was observed at an annual periodicity in MTM and LOWSPEC results across the range of Fe and S time models (Supplements 16, 17). There are several plausible explanations for the absence of an annual signal in the spectral results. First, it is possible that variable sedimentation rates in the study section are not fully captured in the constant-sedimentation-rate modeling methodology. This mismatch, which preferentially influences the high frequencies, could cause the variance associated with an annual signal to be smeared across a broad range of frequencies rather than in a concentrated frequency band. Alternatively, it is possible that the formation of these laminae is not strictly annual, and is instead connected to irregular earth-systems processes acting on subannual to interannual timescales. Additionally, it is possible that at least some of these laminae have no connection to climate if they represent the distal deposits of turbidites, which can form thin couplets that look like varves (Ludlam 1969; Johnson et al. 2018). No obvious graded bedding or turbidite-related sedimentary structures appear in the Upper R-6 zone study interval, and the expanded lake intervals of the Green River Formation, such as the Mahogany zone, appear to contain fewer visible sediment gravity flows (Johnson et al. 2018). However, this does not preclude the presence of finer turbidite deposits in these laminated oil shales (Johnson et al. 2018).

To provide a possible climatic mechanism for the formation of these fine-scale laminae, we propose a depositional model which calls upon changes in lake stratification as a driver for cyclic anoxia of Lake Uinta's bottom waters. For much of the deposition of the Parachute Creek Member, Lake Uinta was likely salinity stratified, with a more dense, saline monimolimnion underlying a fresher epilimnion (Smith and Lee 1982; Johnson et al. 2018). A lack of freshwater fish and mollusk fossils in the Upper R-6 zone strengthens the evidence that the lake waters were saline in composition during its deposition (Vanden Berg and Birgenheier 2016). Variations in this salinity could serve as a mechanism for changes in the

strength of stratification in the lake. We envision that these lamina couplets were produced on subannual to interannual timescales, with their formation strongly driven by processes of evaporation and water input acting on the lake. These combined evaporation and water-input factors influenced the strength of stratification, the positioning of the chemocline in the water column, and the depth and extent of the lake (Fig. 12). These processes have a strong seasonal influence, but irregular variations in evaporation and water input in a season due to natural variations in climate could potentially generate subseasonal to interannual lamina.

In the summer, Lake Uinta would have generally experienced stronger evaporative processes and reduced water input into the lake basin from its catchment area, leading to a shallowing and shrinking of the lake. The increased overall salinity of the lake resulting from this downsizing would have acted to weaken salinity stratification, allowing the depth of Lake Uinta's chemocline to rise in response to enhanced mixing (Fig. 12). With more of the lake bottom's area falling below the chemocline during this seasonal configuration, organic-rich sediments were more likely to be preserved due to the reduced amount of oxygen present below the chemocline. Therefore, we infer that the darker, more organic- and S-enriched lamina were formed under these conditions.

During the winter season, evaporation processes were likely weaker due to cooler temperatures, and early Eocene regional coupled climate models suggest enhanced precipitation input to the Green River Formation basins from Pacific storms (Sewall and Sloan 2006). While some mixing would have occurred, the addition of this fresh water input into the surface waters of the saline lake would have strengthened lake stratification, increasing the density contrast between the now fresher epilimnion and the underlying monimolimnion. This stronger density gradient would have acted to reduce lake overturning and deepen the chemocline of the lake (Fig. 12). During these winter months, we infer that the lighter-colored, more carbonate- and iron-rich laminae were formed in these more oxygenated, less saline waters through precipitation as Ca-, Mg-, and Fe-rich riverine input mixed with alkaline lake waters. The low permeability of the carbonate muds that make up these laminated oil shales and carbonate mudstone facies may have been one factor that aided in the continued preservation of the underlying more organic-rich lamina.

It is important to note that the model we propose is based on our analysis of the Upper R-6 zone, which was deposited as Lake Uinta was reaching its maximum extent in the early Eocene. This model may have utility in understanding Green River Formation laminites which formed under similar paleo-environmental conditions; however, caution must be exercised when applying this model to deposits from more restricted periods of Lake Uinta, when marginal shelves were more prominent due to lower lake levels and sediment gravity flows and other mass-transport processes exerted a stronger influence on deposition (Johnson et al. 2018).

CONCLUSIONS

In this study, the application of XRF and micro-XRF techniques, in combination with available radioisotopic ages, provides the opportunity to evaluate an interval of the well-studied Green River Formation oil shale with a new level of detail. This fresh perspective permits the testing of long-proposed forcing hypotheses, of the paleo-environmental significance of sedimentary rhythms, and of potential linkages between high- and low-frequency forcing.

At the finest scale, laminae in the Upper R-6 zone of the Parachute Creek Member are most strongly associated with changes in lake redox state, reflecting variations in Fe and S that are consistent with annual stratification of the lake and changes in the depth of the lake chemocline. In contrast, variations in deposition of silicate and carbonate appear to be dominated by interdecadal to millennial rhythms, suggesting changes in precipitation and sediment delivery to the paleo-lake (Fig. 11). While no strong support was found for ENSO or sunspot-scale cyclicity in this Upper R-6 zone record, new evidence for a redox-driven origin for laminae provides key insights into the seasonal dynamics of this paleo-lake during the EECO greenhouse climate.

Additionally, punctuated intervals of non-detrital Si deposition with an interdecadal to millennial rhythmicity were identified in micro-XRF and XRF data (Fig. 11). Based on the lack of evidence for a direct biogenic, volcanogenic, or siliciclastic source, this non-detrital Si is thought to be authigenic in origin and connected to changes in pore-water chemistry resulting from organic-matter decomposition. This decomposition followed conditions of enhanced productivity in the early Eocene paleo-lake.

We observed, at the meter scale, an antithetic relationship between carbonate and silicate components of the Skyline 16 core, alternating at a scale consistent with the orbital cycle of precession (Figs. 4, 11). Intervals of non-detrital Si deposition, such as the one identified in our high-resolution scan, appear to most strongly align with one phase of this proposed precession beat (Figs. 10, 11), illustrating how a long-term astronomical cycle manifested in the form of much shorter interdecadal to millennial scale cyclicity.

SUPPLEMENTAL MATERIALS

Supplemental materials are available from SEPM's data archive: https://www.sepm.org/supplemental-materials.

ACKNOWLEDGMENTS

We thank Mike Smith, Brad Singer, Clay Kelly, and Zhengyu Liu for their discussions over the course of this project. This paper benefited from helpful feedback from Linda Hinnov, Ronald Johnson, Brenda Bowen, and John Southard. Additionally, we would like to thank the Utah Geological Survey and the University of Utah's Institute for Clean and Secure Energy for access to the Skyline 16 core. This study received financial support from the National Science Foundation Faculty Early Career Development Program (NSF-EAR 1151438), the National Science Foundation Integrated Earth Systems Program (NSF-EAR 1813278), the Geological Society of America Graduate Student Research Grant program, BP America Inc., and the Department of Geoscience at the University of Wisconsin–Madison.

REFERENCES

Abbott, W., 1957, Tertiary of the Uinta Basin: Guidebook to the geology of the Uinta Basin: Intermountain Association of Petroleum Geologists, Eighth Annual Field Conference, p. 102–109.

Aswasereelert, W., Meyers, S.R., Carroll, A.R., Peters, S.E., Smith, M.E., and Feigl, K.L., 2013, Basin-scale cyclostratigraphy of the Green River Formation, Wyoming: Geological Society of America, Bulletin, v. 125, p. 216–228.

Barker, P., Fontes, J.C., and Gasse, F., 1994, Experimental dissolution of diatom silica in concentrated salt solutions and implications for paleoenvironmental reconstruction: Limnology and Oceanography, v. 39, p. 99–110.

Birgenheier, L.P., and Vanden Berg, M.D., 2011, Core-based integrated sedimentologic, stratigraphic, and geochemical analysis of the oil shale bearing Green River Formation, Uinta Basin, Utah: Topical Report submitted to the U.S. Department of Energy, Natural Energy Laboratory, DE-FE0001243.

Birgenheier, L.P., Vanden Berg, M.D., Plink-Björklund, P., Gall, R.D., Rosencrans, E., Rosenberg, M.J., Toms, L.C., and Morris, J., 2019, Climate impact on fluvial-lake system evolution, Eocene Green River Formation, Uinta Basin, Utah, USA: Geological Society of America, Bulletin, v. 132, p. 562–587.

Bradbury, J.P., and Krebs, W.N., 1995, Fossil continental diatoms: paleolimnology, evolution, and biochronology, *in* Blome, C.D., et al., Siliceous Microfossils: The Paleontological Society, Short Courses in Paleontology, v. 8, p. 119–138.

Bradley, W.H., 1929, The Varves and Climate of the Green River Epoch: U.S. Geological Survey, Professional Paper 496A, 110 p.

Bradley, W.H., and Eugster, H.P., 1969, Geochemistry and paleolimnology of the trona deposits and associated authigenic minerals of the Green River Formation of Wyoming: U.S. Geological Survey, Professional Paper 496-B, 71 p.

Carroll, A.R., and Bohacs, K.M., 1999, Stratigraphic classification of ancient lakes: balancing tectonic and climatic controls: Geology, v. 27, p. 99–102.

Cashion, W.B., 1995, Stratigraphy of the Green River Formation, eastern Uinta Basin, Utah and Colorado, *in* Averett, M.R., ed., The Green River Formation in Piceance Creek and

eastern Uinta Basins: Grand Junction Geological Society, Field Trip Guidebook, p. 15–21.

Cashion, W.B., and Donnell, J.R., 1972, Chart showing correlation of selected key units in the organic-rich sequence of the Green River Formation, Piceance Creek basin, Colorado, and Uinta Basin, Utah: U.S. Geological Survey, Oil and Gas Investigation Chart, Report 65.

Cole, R., 1998, Possible Milankovitch cycles in the Lower Parachute Creek Member of the Green River Formation (Eocene), North-Central Piceance Creek Basin, Colorado: an analysis, *in* Pitman, J., and Carroll, A., eds., Modern and Ancient Lake Systems: Utah Geological Association, Guidebook 26, p. 233–259.

Coney, P.J., and Reynolds, S.J., 1977, Cordilleran Benioff zones: Nature, v. 270, p. 403.

Crowley, K.D., Duchon, C.E., and Rhi, J., 1986, Climate record in varved sediments of the Eocene Green River Formation: Journal of Geophysical Research, v. 91, p. 8637–8647.

Crundwell, F.K., 2014, The mechanism of dissolution of minerals in acidic and alkaline solutions: Part II Application of a new theory to silicates, aluminosilicates and quartz: Hydrometallurgy, v. 149, p. 265–275.

Davis, S.J., Wiegand, B.A., Carroll, A.R., and Chamberlain, C.P., 2008, The effect of drainage reorganization on paleoaltimetry studies: an example from the Paleogene Laramide foreland: Earth and Planetary Science Letters, v. 275, p. 258–268.

Davis, S.J., Mulch, A., Carroll, A.R., Horton, T.W., and Chamberlain, C.P., 2009, Paleogene landscape evolution of the central North American Cordillera: developing topography and hydrology in the Laramide foreland: Geological Society of America, Bulletin, v. 121, p. 100–116.

Dickinson, W.R., and Snyder, W.S., 1978, Plate tectonics of the Laramide orogeny, *in* Matthews, V., III, ed., Laramide folding associated with basement block faulting in the western United States: Geological Society of America, Memoir 151, p. 355–366.

Dickinson, W.R., Klute, M.A., Hayes, M.J., Janecke, S.U., Lundin, E.R., McKittrick, M.A., and Olivares, M.D., 1988, Paleogeographic and paleotectonic setting of Laramide sedimentary basins in the central Rocky Mountain region: Geological Society of America, Bulletin, v. 100, p. 1023–1039.

Donnell, J.R., and Blair, R.W.J., 1970, Resource appraisal of three rich oil-shale zones in the Green River Formation, Piceance Creek Basin, Colorado: Colorado School of Mines Quarterly, v. 65, no. 4, p. 73–87.

Dove, P.M., and Rimstidt, J.D., 1994, Silica–water interactions, *in* Heaney, P.J., ed., Silica: Physical Behavior, Geochemistry, and Materials Applications: Mineralogical Society of America, Reviews in Mineralogy, v. 29, 606 p.

Dyni, J.R., 1976, Trioctahedral Smectite in the Green River Formation, Duchesne County, Utah: U.S. Geological Survey, Professional Paper 967, 14 p.

Fischer, A.G., and Roberts, L.T., 1991, Cyclicity in the Green River Formation (lacustrine Eocene) of Wyoming: Journal of Sedimentary Petrology, v. 61, p. 1146–1154.

Flower, R.J., and Ryves, D.B., 2009, Diatom preservation: differential preservation of sedimentary diatoms in two saline lakes: Acta Botanica Croatica, v. 68, p. 381–399.

Glenn, C.R., and Kelts, K., 1991, Sedimentary rhythms in lake deposits, *in* Einsele, G., Ricken, W., and Seilacher, A., eds., Cycles and Events in Stratigraphy: New York, Springer-Verlag, p. 188–221.

Horsfield, B., Curry, D.J., Bohacs, K., Littke, R., Rullkötter, J., Shenk, H.J., Radke, M., Schaefer, R.G., Carroll., A.R., Isaksen, G., and Witte, E.G., 1994, Organic geochemistry of freshwater and alkaline lacustrine sediments in the Green River Formation of the Washakie Basin, Wyoming, USA: Organic Geochemistry, v. 22, p. 415–440.

Hosterman, J.W., and Dyni, J.R., 1972, Clay mineralogy of the Green River Formation, Piceance Creek Basin: a preliminary study: U.S. Geological Survey, Professional Paper 800-D, p. 159–163.

Johnson, R.C., 1984, New Names for Units in the Lower Part of the Green River Formation, Piceance Creek Basin, Colorado: U.S. Geological Survey, Bulletin 1529-1, 26 p.

Johnson, R.C., 1985, Early Cenozoic History of the Uinta and Piceance Creek Basins, Utah and Colorado, with Special Reference to the Development of Eocene Lake Uinta, *in* Flores, R.M., and Kaplan, S.S., eds., Cenozoic Paleogeography of Western United States: SEPM, Rocky Mountain Section, p. 247–276.

Johnson, R.C., and Brownfield, M.E., 2015, Development, evolution, and destruction of the saline mineral area of Eocene Lake Uinta, Piceance Basin, western Colorado: U.S. Geological Survey, Scientific Investigations Report, Numbered Series 2013–5176, 87 p.

Johnson, R.C., Birdwell, J.E., and Mercier, T., 2018, Controls on organic matter distributions in Eocene Lake Uinta, Utah and Colorado: The Mountain Geologist, v. 55, p. 177–216.

Johnson, R.C., Birdwell, J.E., Brownfield, M.E., Mercier, T.J., and Hansley, P.L., 2019, Connections between Eocene lakes Uinta and Gosiute with emphasis on the infilling stage of Lake Uinta in Piceance Basin: The Mountain Geologist, v. 56, p. 143–183.

Johnson, T.C., 1984, Sedimentation in large lakes: Annual Review of Earth and Planetary Sciences, v. 12, p. 179–204.

Knauss, K.G., and Wolery, T.J., 1988, The dissolution kinetics of quartz as a function of pH and time at 70°C: Geochimica et Cosmochimica Acta, v. 52, p. 43–53.

Krebs, W., 1994, The biochronology of freshwater planktonic diatom communities in western North America, *in* Kociolek, J.P., ed., Proceedings of the 11th International Diatom Symposium: California Academy of Sciences, San Francisco, p. 485–499.

Lohman, K.E., and Andrews, G.W., 1968, Late Eocene Nonmarine Diatoms from the Beaver Divide Area Fremont County, Wyoming: U.S. Geological Survey, Professional Paper 593E, 38 p.

Ludlam, S.D., 1969, Fayetteville Green Lake, New York. 3. The Laminated Sediments: Limnology and Oceanography, v. 14, p. 848–857.

Ma, C., Meyers, S.R., Sageman, B.B., Singer, B.S., and Jicha, B.R., 2014, Testing the astronomical time scale for Oceanic Anoxic Event 2, and its extension into Cenomanian strata of the Western Interior Basin (USA): Geological Society of America, Bulletin, v. 126, p. 974–989.

Machlus, M.L., Olsen, P.E., Christie-Blick, N., and Hemming, S.R., 2008, Spectral analysis of the lower Eocene Wilkins Peak Member, Green River Formation, Wyoming: support for Milankovitch cyclicity: Earth and Planetary Science Letters, v. 268, p. 64–75.

Machlus, M.L., Ramezani, J., Bowring, S.A., Hemming, S.R., Tsukui, K., and Clyde, W.C., 2015, A strategy for cross-calibrating U–Pb chronology and astrochronology of sedimentary sequences: an example from the Green River Formation, Wyoming, USA: Earth and Planetary Science Letters, v. 413, p. 70–78.

Meyers, S.R, 2008, Resolving Milankovitchian controversies: the Triassic Latemar Limestone and the Eocene Green River Formation: Geology, v. 36, p. 319–322.

Meyers, S.R., 2012, Seeing red in cyclic stratigraphy: spectral noise estimation for astrochronology: Paleoceanography, v. 27, no. PA3228.

Meyers, S.R., 2014, Astrochron: An R Package for Astrochronology: https://cran.r-project.org/package=astrochron

Meyers, S.R., Sageman, B.B., and Hinnov, L.A., 2001, Integrated quantitative stratigraphy of the Cenomanian–Turonian Bridge Creek Limestone Member using evolutive harmonic analysis and stratigraphic modeling: Journal of Sedimentary Research, v. 71, p. 628–644.

Morgan, C.D., Chidsey, T.C., Jr., McClure, K.P., Bereskin, S.R., and Deo, M.D., 2003, Reservoir Characterization of the Lower Green River Formation, Uinta Basin, Utah: Utah Geological Survey, Open File Report 411, 142 p.

Mustoe, G.E., 2005, Diatomaceous origin of siliceous shale in Eocene lake beds of central British Columbia: Canadian Journal of Earth Sciences, v. 42, p. 231–241.

North, S.M., Stockhecke, M., Tomonaga, Y., and Mackay, A.W., 2018, Analysis of a fragmentary diatom record from Lake Van (Turkey) reveals substantial lake-level variability during previous interglacials MIS7 and MIS5e: Journal of Paleolimnology, v. 59, p. 119–133.

Picard, M.D., and High, L.R., 1972, Paleoenvironmental reconstructions in an area of rapid facies change, Parachute Creek Member of Green River Formation (Eocene), Uinta Basin, Utah, Geological Society of America, Bulletin, v. 83, p. 2689–2708.

Pietras, J.T., Carroll, A.R., Singer, B.S., and Smith, M.E., 2003, 10 k.y. depositional cyclicity in the early Eocene: Stratigraphic and $^{40}Ar/^{39}Ar$ evidence from the lacustrine Green River Formation: Geology, v. 31, p. 593–596.

R Core Team, 2014, R: a language and environment for statistical computing: Vienna, R Foundation for Statistical Computing.

Reimer, A., Landmann, G., and Kempe, S., 2009, Lake Van, Eastern Anatolia, hydrochemistry and history: Aquatic Geochemistry, v. 15, p. 195–222.

Remy, R.R., 1992, Stratigraphy of the Eocene part of the Green River Formation in the south-central part of the Uinta Basin, Utah: U.S. Geological Survey, Bulletin Report 1787BB.

Rhodes, M.K., Carroll, A.R., Pietras, J.T., Beard, B.L., and Johnson, C.M., 2002, Strontium isotope record of paleohydrology and continental weathering, Eocene Green River Formation, Wyoming: Geology, v. 30, p. 167–170.

Ripepe, M., Roberts, L.T., and Fischer, A.G., 1991, ENSO and sunspot cycles in varved Eocene oil shales from image analysis: Journal of Sedimentary Petrology, v. 61, p. 1155–1163.

Robb, W.A., and Smith, J.W., 1974, Mineral profile of the oil shales in Colorado Core Hole No. 1, Piceance Creek Basin, Colorado, *in* Murray, D.K., ed., Guidebook to the Energy Resources of the Piceance Creek Basin Colorado: Rocky Mountain Association of Geologists, Twenty-Fifth Field Conference Guidebook, p. 91–100.

Rosenberg, M.J., Birgenheier, L., and Vanden Berg, M.D., 2015, Facies, Stratigraphic Architecture, and Lake Evolution of the Oil Shale Bearing Green River Formation, Eastern Uinta Basin, Utah, *in* Smith, M., and Carroll, A., eds., Stratigraphy and Paleolimnology of the Green River Formation, Western USA: Syntheses in Limnogeology, v. 1, p. 211–249.

Ryder, R.T., Fouch, T.D., and Elison, J.H., 1976, Early Tertiary sedimentation in the western Uinta Basin, Utah: Geological Society of America, Bulletin, v. 87, p. 496–512.

Ryves, D.B., Battarbee, R.W., Juggins, S., Fritz, S.C., and Anderson, N.J., 2006, Physical and chemical predictors of diatom dissolution in freshwater and saline lake sediments in North America and West Greenland: Limnology and Oceanography, v. 51, p. 1355–1368.

Sageman, B.B., and Hollander, D.J., 1999, Integration of paleoecological and geochemical proxies: a holistic approach to the study of past global change, *in* Johnson, C.J., and Barrera, E., eds., The Evolution of Cretaceous Ocean/Climate Systems: Geological Society of America, Special Paper 332, p. 365–384.

Sageman, B.B., and Lyons, T.W., 2003, Geochemistry of fine-grained sediments and sedimentary rocks, *in* Holland, H.D., and Turekian, K.K., eds., Treatise on Geochemistry: Oxford, Pergamon, p. 115–158.

Sayles, R.W., 1922, The dilemma of the paleoclimatologists: American Journal of Science, Series 5, v. 3, p. 458.

Sewall, J.O., and Sloan, L.C., 2006, Come a little bit closer: a high-resolution climate study of the early Paleogene Laramide foreland: Geology, v. 34, p. 81–84.

Sheliga, C.M., 1980, Sedimentation of the Eocene Green River Formation in Sevier and Sanpete Counties, Utah [M.S. Thesis]: Columbus, The Ohio State University, 166 p.

Sluijs, A., Röhl, U., Schouten, S., Brumsack, H.-J., Sangiorgi, F., Damasté, J.S.S., and Brinkhuis, H., 2008, Arctic late Paleocene–early Eocene paleoenvironments with special emphasis on the Paleocene–Eocene thermal maximum (Lomonosov Ridge, Integrated Ocean Drilling Program Expedition 302): Paleoceanography, v. 23, PA1S11.

Smith, J.W., and Lee, K.K., 1982, Geochemistry and physical paleolimnology of Piceance Creek basin oil shales, *in* Gary, J.H., ed., 15th Oil Shale Symposium, Proceedings: Colorado School of Mines Press, v. 15, p. 101–114.

Smith, M.E., Singer, B.S., and Carroll, A.R., 2003, $^{40}Ar/^{39}Ar$ geochronology of the Eocene Green River Formation, Wyoming: Geological Society of America, Bulletin, v. 115, p. 549–565.

Smith, M.E., Carroll, A.R., and Singer, B.S., 2008, Synoptic reconstruction of a major ancient lake system: Eocene Green River Formation, western United States: Geological Society of America, Bulletin, v. 120, p. 54–84.

Smith, M.E., Chamberlain, K.R., Singer, B.S., and Carroll, A.R., 2010, Eocene clocks agree: coeval $^{40}Ar/^{39}Ar$, U-Pb, and astronomical ages from the Green River Formation, Geology, v. 38, p. 527–530.

Smith, M.E., Carroll, A.R., Jicha, B.R., Cassel, E.J., and Scott, J.J., 2014, Paleogeographic record of Eocene Farallon slab rollback beneath western North America: Geology, v. 42, p. 1039–1042.

Smith, M.E., and Carroll, A.R., 2015, Introduction to the Green River Formation, *in* Smith, M., and Carroll, A., eds., Stratigraphy and Paleolimnology of the Green River Formation, Western USA: Syntheses in Limnogeology, Volume 1: Dordrecht, Springer, p. 1–12.

Surdam, R.C., and Stanley, K.O., 1980, Effects of changes in drainage-basin boundaries on sedimentation in Eocene lakes Gosiute and Uinta of Wyoming, Utah, and Colorado: Geology, v. 8, p. 135–139.

Tänavsuu-Milkeviciene, K., and Sarg, J.F., 2012, Evolution of an organic-rich lake basin-stratigraphy, climate and tectonics: Piceance Creek basin, Eocene Green River Formation: evolution of an organic-rich lake: Sedimentology, v. 59, p. 1735–1768.

Thomson, D.J., 1982, Spectrum estimation and harmonic analysis: Institute of Electrical and Electronics Engineers, Proceedings, v. 70, p. 1055–1096.

Vanden Berg, M.D., and Birgenheier, L.P., 2011, Not All Rich Zones Are Created Equal: Geologic Characterization Results of Green River Formation Core Descriptions from Utah's Uinta Basin, Including the Newly Drilled Skyline 16 Core: 31st Oil Shale Symposium, Golden, Colorado, Oct. 17–19.

Vanden Berg, M.D., and Birgenheier, L.P., 2016, Evaluation of the Upper Green River Formation's Oil Shale Resource in the Uinta Basin, *in* Spinti, J.P., ed., Utah Oil Shale: Science, Technology, and Policy Perspectives: CRC Press, New York, p. 59–82.

Vanden Berg, M.D., and Birgenheier, L.P., 2017, An examination of the hypersaline phases of Eocene Lake Uinta, upper Green River Formation, Uinta Basin, Utah: Journal of Paleolimnology, v. 58, p. 353–371.

Washburn, K.E., Birdwell, J.E., Foster, M., and Gutierrez, F., 2015, Detailed description of oil shale organic and mineralogical heterogeneity via Fourier transform infrared microscopy: Energy & Fuels, v. 29, p. 4264–4271.

Weiss, M.P., Witkind, I.J., and Cashion, W.B., 1990, Geologic map of the Price $30' \times 60'$ quadrangle, Carbon, Duchesne, Uintah, Utah, and Wasatch counties, Utah: U.S. Geological Survey, Miscellaneous Investigations Series, Map I-1981.

Witkind, I.J., 1995, Geologic map of the Price $1° \times 2°$ Quadrangle, Utah: U.S. Geological Survey, Miscellaneous Investigations Series, Map I-2462.

Wolfe, A.P., Edlund, M.B., Sweet, A.R., and Creighton, S.D., 2006, A first account of organelle preservation in Eocene nonmarine diatoms: observations and paleobiological implications: Palaios, v. 21, p. 298–304.

Zachos, J.C., Pagani, M., Sloan, L., Thomas, E., and Billups, K., 2001, Trends, Rhythms, and Aberrations in Global Climate 65 Ma to Present: Science, v. 292, p. 686–693.

Zachos, J.C., Dickens, G.R., and Zeebe, R.E., 2008, An early Cenozoic perspective on greenhouse warming and carbon-cycle dynamics: Nature, v. 451, p. 279–283.

Received 14 May 2019; accepted 11 December 2019.

Queries for sedp-90-03-09

This article has been typeset from the submitted materials. Check proofs carefully for conversion or other inadvertent errors. Please follow the Allen Press Guide to PDF Annotation when marking revisions. Do not edit the PDF directly.

If present, queries will be listed below with corresponding numbers in the margins or may appear as PDF comments addressed to the author or editor. If a correction is desired in response to a query, mark the necessary changes directly in the proof using the appropriate annotation tool. If no change is desired, no action is necessary in response.